Diffractive and photon exchange processes at the LHC[9]

Christophe Royon [e, i, j]

[e]The University of Kansas, Lawrence, USA

[i]Institute of Physics, Academy of Science of the Czech Republic, Prague, Czech Republic

[j]Institute of Nuclear Physics, Polish Academy of Sciences, Krakow, Poland

Abstract

In these lectures, we give a brief description of diffractive and photon exchange physics at the LHC.

1 Experimental definition of diffraction

In this section, we discuss the different experimental ways to define diffraction. As an example, we describe the methods used by the H1 and ZEUS experiments at HERA, DESY, Hamburg in Germany since it is simpler for an ep collider.

1.1 The rapidity gap method

HERA is a collider where electrons of 27.6 GeV collide with protons of 920 GeV. A typical event as shown in the upper plot of Fig. 1 is $ep \to eX$ where electron and jets are produced in the final state. We notice that the electron is scattered in the H1 backward detector[10] (in green) whereas some hadronic activity is present in the forward region of the detector (in the LAr calorimeter and in the forward muon detectors). The proton is thus completely destroyed and the interaction leads to jets and proton remnants directly observable in the detector. The fact that much energy is observed in the forward region is due to colour exchange between the scattered jet and the proton remnants. In about 10% of the events, the situation is completely different. Such events appear like the one shown in the bottom plot of Fig. 46. The electron is still present in the backward detector, there is still some hadronic activity (jets) in the LAr calorimeter, but no energy above noise level is deposited in the forward part of the LAr calorimeter or in the forward muon detectors. In other words, there is no color exchange between the proton and the produced jets. As an example, this can be explained if the proton stays intact after the interaction.

This experimental observation leads to the first definition of diffraction: request a rapidity gap (in other words a domain in the forward detectors where no energy is deposited above noise level) in the forward region. For example, the H1 collaboration requests no energy deposition in the rapidity region $3.3 < \eta < 7.5$ where η is the pseudorapidity. Let us note that this approach does not insure that the proton stays intact after the interaction, but it represents a limit on the mass of the produced object $M_Y < 1.6$ GeV. Within this limit, the proton could be dissociated. The adavantage of the rapidity gap method is that it is quite easy to implement and it has a large acceptance in the diffractive kinematical plane.

[9]Presented at the School "New trends in HEP and QCD", October 21 - November 6 2014, Natal, Brazil.

[10]At HERA, the backward (resp. forward) directions are defined as the direction of the outgoing electron (resp. proton).

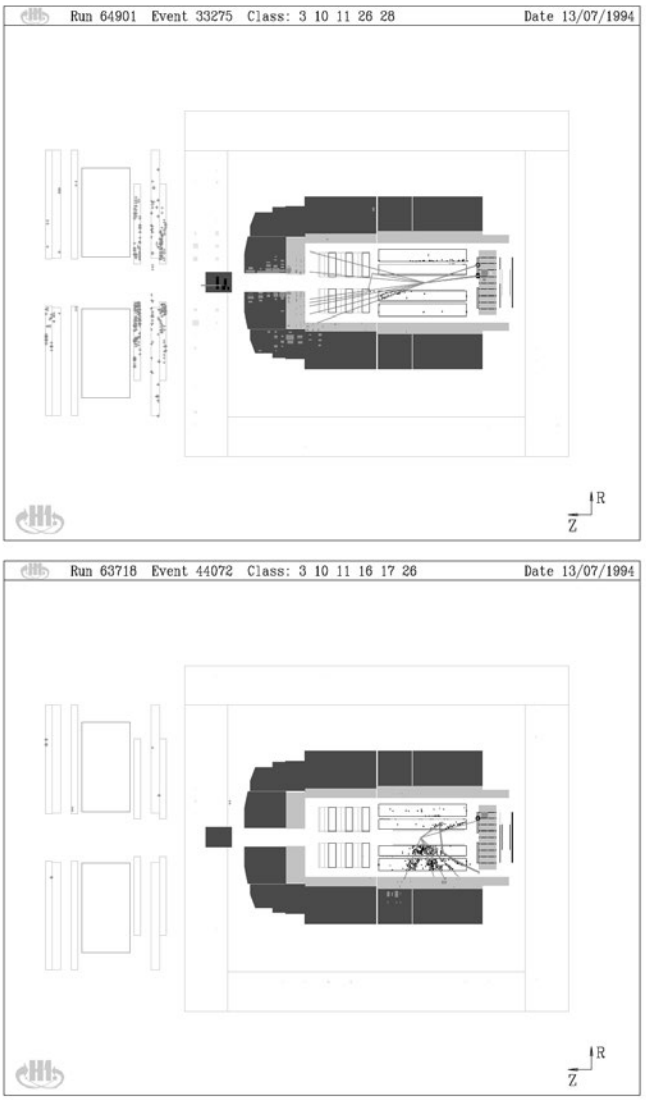

Figure 46: "Usual" and diffractive events in the H1 experiment.

1.2 Proton tagging

The second experimental method to detect diffractive events is also natural: the idea is to detect directly the intact proton in the final state. The proton loses a small fraction of its energy and is thus scattered at very small angle with respect to the beam direction. Some special detectors called roman pots can be used to detect the protons close to the beam. The basic idea is simple: the roman pot detectors are located far away from the interaction point and can move close to the beam, when the beam is stable, to detect protons scattered at vary small angles. The inconvenience is that the kinematical reach of those detectors is much smaller than with the rapidity gap method. On the other hand, the advantage is that it gives a clear signal of diffraction since it measures the diffracted proton directly.

A scheme of a roman pot detector as it is used by the H1 or ZEUS experiment is shown in Fig. 47. The beam is the horizontal line at the upper part of the figure. The detector is located in the pot itself and can move closer to the beam when the beam is stable enough (during the injection period, the detectors are protected in the home position). Step motors allow to move the detectors with high precision. A precise knowledge of the detector position is necessary to reconstruct the transverse

momentum of the scattered proton and thus the diffractive kinematical variables. The detectors are placed in a secondary vaccuum with respect to the beam one.

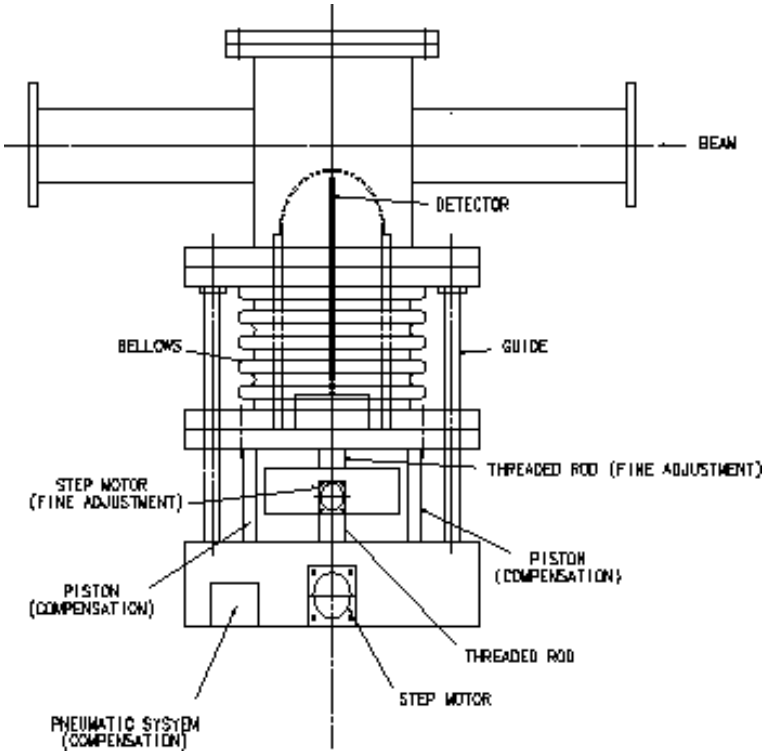

Figure 47: Scheme of a roman pot detector.

1.3 Diffractive kinematical variables

After having described the different experimental definitions of diffraction at HERA, we will give the new kinematical variables used to characterise diffraction. A typical diffractive event is shown in Fig. 48 where $ep \to epX$ is depicted. In addition to the usual deep inelastic variables, Q^2 the transfered energy squared at the electron vertex, x the fraction of the proton momentum carried by the struck quark, $W^2 = Q^2(1/x - 1)$ the total energy in the final state, new diffractive variables are defined: x_P (called ξ at the Tevatron and the LHC) is the momentum fraction of the proton carried by the colourless object called the pomeron, and β the momentum fraction of the pomeron carried by the interacting parton inside the pomeron if we assume the pomeron to be made of quarks and gluons:

$$x_P = \xi = \frac{Q^2 + M_X^2}{Q^2 + W^2} \tag{144}$$

$$\beta = \frac{Q^2}{Q^2 + M_X^2} = \frac{x}{x_P}. \tag{145}$$

2 Diffractive structure function measurement at HERA

2.1 Diffractive factorisation

In the following diffractive structure function analysis, we distinguish two kinds of factorisation at HERA. The first factorisation is the QCD hard scattering collinear factorisation at fixed x_P and t (see left plot of Fig. 49) [1], namely

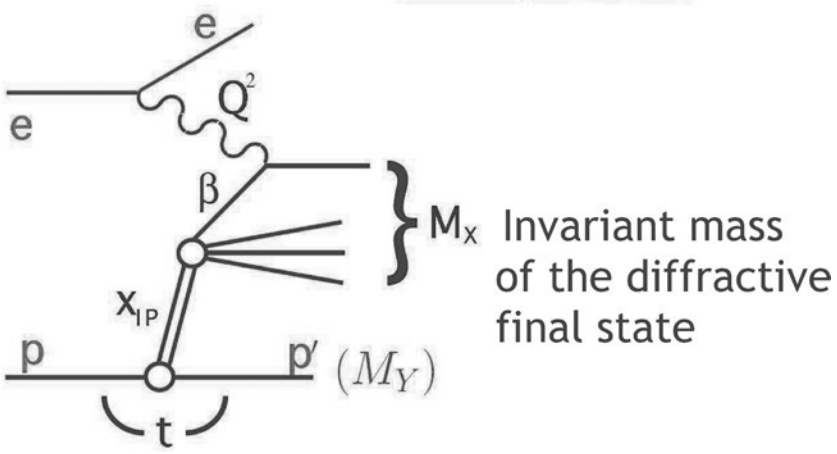

Figure 48: Scheme of a diffractive event at HERA.

$$d\sigma(ep \to eXY) = f_D(x, Q^2, x_P, t) \times d\hat{\sigma}(x, Q^2) \tag{146}$$

where we can factorise the flux f_D from the cross section $\hat{\sigma}$. This factorisation was proven recently, and separates the γq coupling to the interaction with the colourless object.

The Regge factorisation at the proton vertex allows to factorise the (x_P, t) and (β, Q^2) dependence, or in other words the hard interaction from the pomeron coupling to the proton (see right plot of Fig. 49).

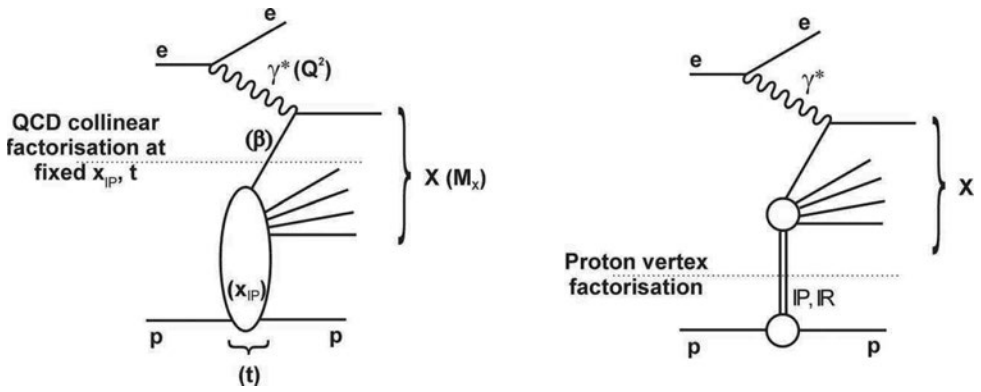

Figure 49: Diffractive factorisation.

2.2 Measurement of the diffractive proton structure function

The different measurements are performed using the three different methods to define diffractive events described in the first section. As an example, the H1 collaboration measures the diffractive cross section σ^D using the rapidity gap method:

$$\frac{d^3\sigma^D}{dx_P dQ^2 d\beta} = \frac{2\pi\alpha_{em}^2}{\beta Q^4}\left(1 - y + \frac{y^2}{2}\right)\sigma_r^D(x_P, Q^2, \beta) \tag{147}$$

where σ_r^D is the reduced diffractive cross section. The measurement [2] is presented in Fig. 50. We notice that the measurement has been performed with high precision over a wide kinematical domain:

$0.01 < \beta < 0.9$, $3.5 < Q^2 < 1600$ GeV^2, $10^{-4} < x_P < 5.10^{-2}$. The data are compared to the result of a QCD fit which we will discuss in the following.

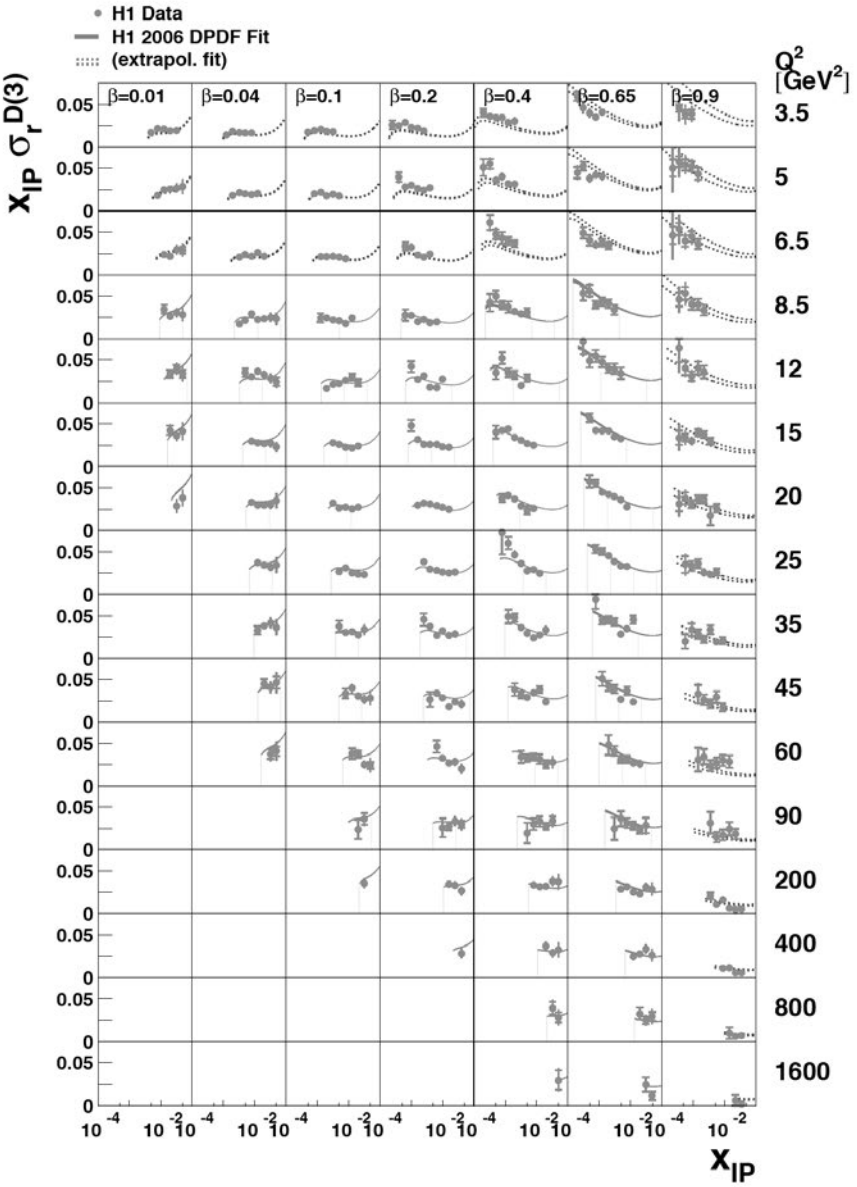

Figure 50: Measurement of the diffractive structure function by the H1 collaboration.

The rapidity gap data are also compared with the data obtained either using the M_X method or the one using proton tagging in roman pot detectors. Since they do not correspond exactly to the same definition of diffraction, a correction factor of 0.85 must be applied to the ZEUS M_X method to be compared to the rapidity gap one (this factor is due to the fact that the two methods correspond to two different regions in M_Y, namely $M_Y < 1.6$ GeV for H1 and $M_Y < 2.3$ GeV for ZEUS). It is also possible to measure directly in the H1 experiment the ratio of the diffractive structure function measurements between the rapidity gap and the proton tagging methods as illustrated in Fig. 51. Unfortunately, the measurement using the proton tagging method is performed only in a restricted kinematical domain. No kinematical dependence has been found within uncertainties for this ratio inside this kinematical domain (see Fig. 51 for the β and Q^2 dependence, and Ref. [3] for the x_P

dependence as well). Note that the ratio could still be depending on β and Q^2 outside the limited domain of measurement.

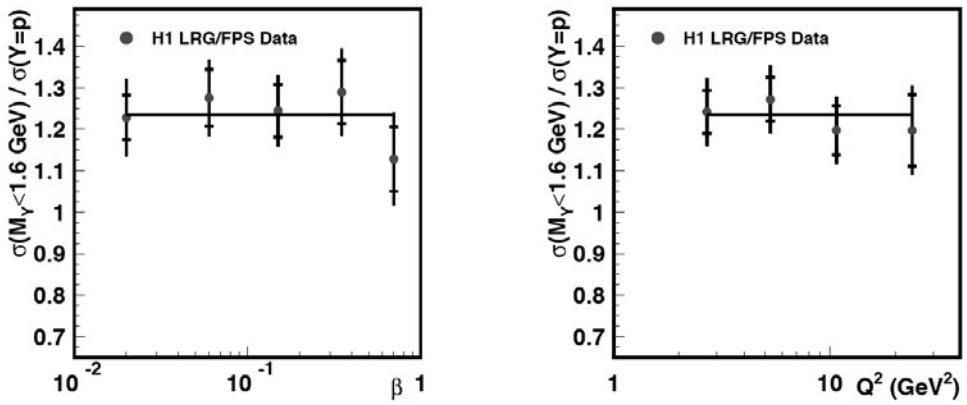

Figure 51: Measurement of the ratio of the diffractive structure function between the rapidity gap and the proton tagging methods (H1 experiment).

2.3 QCD analysis of the diffractive structure function measurement

As we mentionned already, according to Regge theory, we can factorise the (x_P, t) dependence from the (β, Q^2) one. The first diffractive structure function measurement from the H1 collaboartion [4] showed that this assumption was not true. The natural solution as observed in soft physics was that two different trajectories, namely pomeron and secondary reggeon, were needed to describe the measurement, which lead to a good description of the data. The diffractive structure function then reads:

$$F_2^D \sim f_p(x_P)(F_2^D)_{Pom}(\beta, Q^2) + f_r(x_P)(F_2^D)_{Reg}(\beta, Q^2) \tag{148}$$

where f_p and f_r are the pomeron and reggeon fluxes, and $(F_2^D)_{Pom}$ and $(F_2^D)_{Reg}$ the pomeron and reggeon structure functions. The flux parametrisation is predicted by Regge theory:

$$f(x_P, t) = \frac{e^{B_P t}}{x_P^{2\alpha_P(t)-1}} \tag{149}$$

with the following pomeron trajectory

$$\alpha_P(t) = \alpha_P(0) + \alpha'_P t. \tag{150}$$

The t dependence has been obtained using the proton tagging method, and the following values have been found: $\alpha'_P = 0.06^{+0.19}_{-0.06}$ GeV^{-2}, $B_P = 5.5^{+0.7}_{-2.0}$ GeV^{-2} (H1). Similarly, the values of $\alpha_P(0)$ have been measured using either the rapidity gap for H1 or the M_X method for ZEUS in the QCD fit described in the next paragraph [2, 5]. The Reggeon parameters have been found to be $\alpha'_R = 0.3$ GeV^{-2}, $B_R = 1.6$ GeV^{-2} (H1). The value of $\alpha_R(0)$ has been determined from rapidity gap data and found to be equal to 0.5. Since the reggeon is expected to have a similar $q\bar{q}$ structure as the pion and the data are poorly sensitive to the structure function of the secondary reggeon, it was assumed to be similar to the pion structure with a free normalisation.

The next step is to perform Dokshitzer Gribov Lipatov Altarelli Parisi (DGLAP) [6] fits to the pomeron structure function. If we assume that the pomeron is made of quarks and gluons, it is natural to check whether the DGLAP evolution equations are able to describe the Q^2 evolution of these parton densities. As necessary for DGLAP fits, a form for the input distributions is assumed at a given Q_0^2 and is evolved using the DGLAP evolution equations to a different Q^2, and fitted to the diffractive structure function data at this Q^2 value. The form of the distribution at Q_0^2 has been chosen to be:

$$\beta q = A_q \beta^{B_q} (1-\beta)^{C_q} \quad (151)$$
$$\beta G = A_g (1-\beta)^{C_g}, \quad (152)$$

leading to three (resp. two) parameters for the quark (resp. gluon) densities. At low β, the evolution is driven by $g \to q\bar{q}$ while $q \to qg$ becomes more important at high β. All diffractive data with $Q^2 > 8.5$ GeV^2 and $\beta < 0.8$ have been used in the fit [2,5] (the high β points being excluded to avoid the low mass region where the vector meson resonances appear). This leads to a good description of all diffractive data included in the fit.

The DGLAP QCD fit allows to get the parton distributions in the pomeron as a direct output of the fit, and is displayed in Fig. 52 as a blue shaded area as a function of β. We first note that the gluon density is much higher than the quark one, showing that the pomeron is gluon dominated. We also note that the gluon density at high β is poorly constrained which is shown by the larger shaded area.

Another fit was also performed by the H1 collaboration imposing $C_g = 0$. While the fit quality is similar, the gluon at high β is quite different, and is displayed as a black line in Fig. 52 (z is the equivalent of β for quarks). This shows further that the gluon is very poorly constrained at high β and some other data sets such as jet cross section measurements are needed to constrain it further.

3 Diffraction at the LHC

The LHC is a pp collider located close to Geneva, at CERN, Switzerland. It is presently the collider with the highest center-of-mass energy of about 13 TeV.

3.1 Diffractive kinematical variables

The difference between diffraction at HERA and at the Tevatron is that diffraction can occur not only on either p side as at HERA, but also on both sides. The former case is called single diffraction whereas the other one double pomeron exchange. In the same way as we defined the kinematical variables x_P and β at HERA, we define $\xi_{1,2}(=x_P$ at HERA) as the proton fractional momentum loss (or as the p momentum fraction carried by the pomeron), and $\beta_{1,2}$, the fraction of the pomeron momentum carried by the interacting parton. The produced diffractive mass is equal to $M^2 = s\xi_1$ for single diffractive events and to $M^2 = s\xi_1\xi_2$ for double pomeron exchange. The size of the rapidity gap is of the order of $\Delta\eta \sim \log 1/\xi_{1,2}$.

The rapidity gap method can be only used at low luminosity at the LHC. At high instantaneous luminosity, many interactions (called pile up) occur within the same bunch crossing. The pile up interactions will fill in the rapidity gap devoid of any energy, making difficult to use the rapidity gap method. It is thus preferable to tag directly the protons at the LHC.

3.2 Diffraction at the LHC

In this short report we discuss some potential measurements that can be accomplished in forward physics at the LHC. We distinguish between the low luminosity (no pile up), medium luminosity

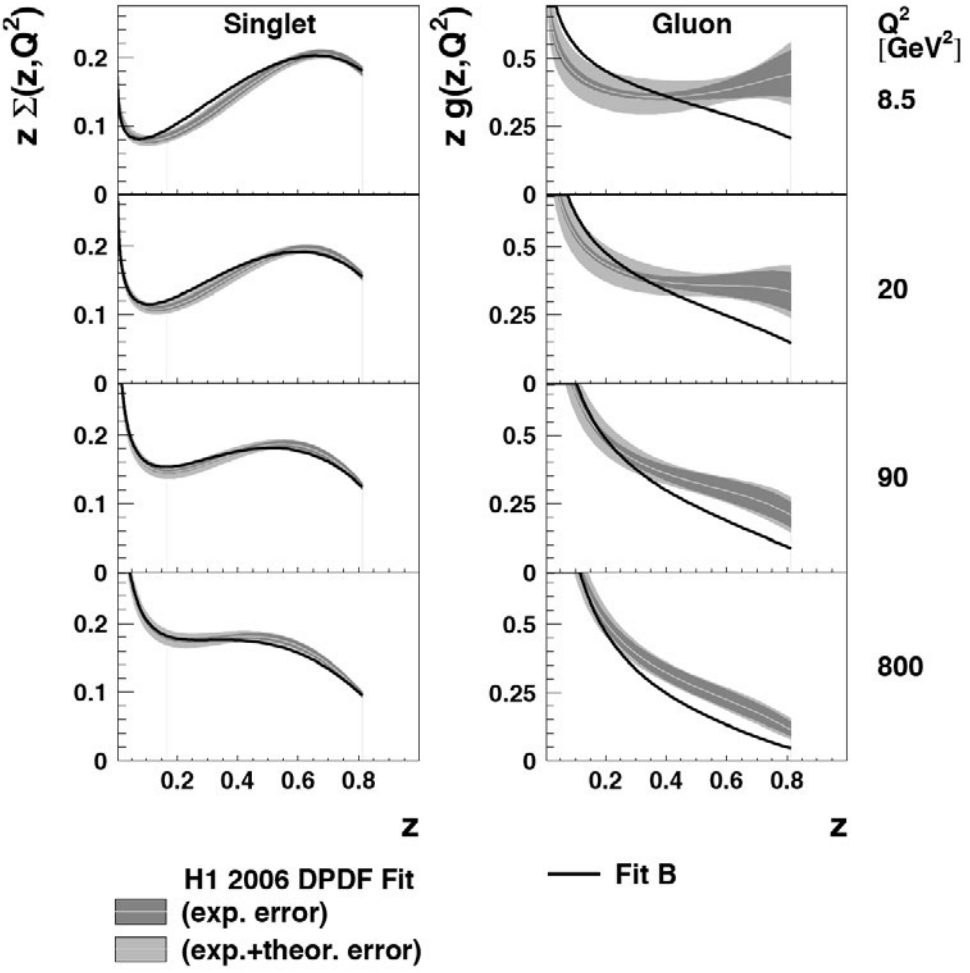

Figure 52: Extraction of the parton densities in the pomeron using a DGLAP NLO fit (H1 collaboration).

(moderate pile up) and high luminosity (high pile up) environments. Forward physics is fundamental at the LHC since it adresses the QCD dynamics at the interface between hard and soft physics. For instance, the soft total pp cross section probes long transverse distances, and the BFKL pomeron is valid at short distances. Most of the energy in a standard pp collision goes in the forward direction and not in the central one, and it is important to tune the MC expectations for a good understanding of the event topology. In addition, diffraction and especially photon exchange processes allow performing searches beyond the standard model. Further more, diffractive events are important to tune MC and understand underlying events and soft QCD. Almost all Monte Carlo are designed for hard processes and new physics, and they have difficulties with incorporating diffraction and need improvement. Diffractive measurements are fundamental to achieve this goal. More details about the different measurements can be found in [7].

3.3 LHC running conditions and forward detectors

Forward detectors

At the LHC, the different detectors are sensitive to different programs of forward physics. The LHCf detector [8] measures the multiplicities and energy flow in the very forward direction at very low luminosity. The selection of diffractive events in LHCb [9] and Alice [10] is performed by using the so-called rapidity gap method and will benefit from new scintillators that cover the forward region as was installed previously in CMS. The present coverage of the CMS and ATLAS forward detectors will be complemented by the AFP and CMS-TOTEM/CT-PPS projects to add additional proton detectors at about 220 meters from the interaction point [11, 12].

Running at low and high β^* using the CMS-TOTEM, CT-PPS and ATLAS-AFP detectors allows accessing different kinematical domains for diffraction. In Fig. 53 are dispalyed the acceptances in proton relative energy loss ξ versus the proton transverse momentum p_T for two values of β^* (0.65 m, the nominal collision optics, and 90 m) for vertical (ALFA) or horizontal (AFP) roman pot detector configurations located about 220 m from the ATLAS interaction point. We notice that one can access low and high mass diffraction (low and high ξ) at high β^* in ALFA and only low mass diffraction (up to $\xi \sim 0.15$) at low β^* using AFP. Both measurements will be thus interesting in order to cover easily low and high mass diffraction. The kinematical coverage is similar for the vertical (CMS-TOTEM) and the horizontal pots (CT-PPS) of CMS and TOTEM.

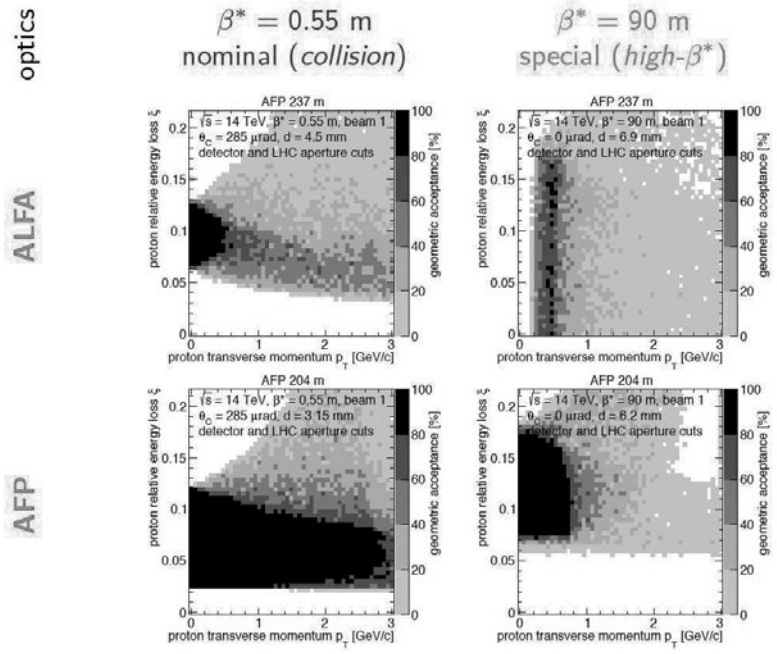

Figure 53: Acceptance ξ versus t at low and high β^* for vertical (ALFA) and horizontal (AFP) roman pots at 220 m.

Different luminosity conditions

As we mentioned in the last section, we distinguish between the low, medium and high luminosity runs.

The low luminosity runs (without pile up) allow performing multiplicity and energy flow measurements useful to tune MC as well as to measure the total and soft diffractive cross sections in the ATLAS/ALFA and TOTEM experiments. Additional measurements such as single diffraction, low

mass resonances and glueballs typically require a few days of data taking (0.1 to 1. pb^{-1}).

Medium luminosity runs are specific for the different LHC experiments. LHCb accumulate typically a few fb^{-1} at low pile up during their nominal data taking while the CMS-TOTEM and ATLAS (ALFA and AFP) can accumulate low pile up data in low and high β^* special runs at low luminosity at the LHC. It is then typically possible to accumulate 1 to 10 pb^{-1} at high β^* with a pile up $\mu \sim 1$ with a few days of data taking and 10 to 100 pb^{-1} at low β^* with one to two weeks of data taking at $\mu \sim 2$ to 5.

High pile up data taking means taking all the luminosity delivered typically to ATLAS and CMS with a pile up μ between 20 and 100. It is also possible to collect data at a lower pile up $\mu \sim 25$ by restricting to end of store data taking (up to 40% of the total luminosity can be collected in this way). or to data originating from the tails of the vertex distribution.

3.4 Low luminosity measurements

In addition to measurements of the total and soft diffraction cross sections performed at high β^* in dedicated runs, data taken without pile up are specially interesting to measure multiplicities and energy flow especially useful to tune MC benefitting from the different coverage in rapidity of the different LHC experiments. There is also a special interested especially driven by the cosmic ray community to measure the multiplicities in proton-oxygen runs at the LHC since models make different predictions in those conditions even if they lead to similar predictions in proton proton interactions at 14 TeV. This will allow making precise predictions on proton oxygen events for cosmic ray physics.

Another example of fundamental measurements to be performed at very low luminosity is the measurement of the size of the forward gap in diffractive events when the protons are tagged in AFP or in TOTEM. The differences between the models are much larger when the protons are tagged [13], and this will allow further tuning of the models as shown in Fig. 54.

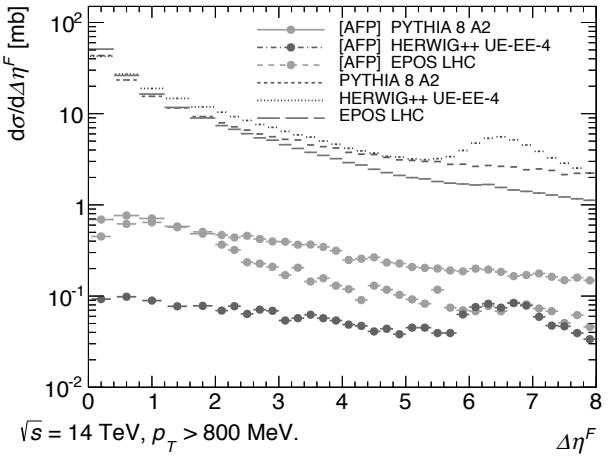

Figure 54: Size of rapidity in diffractive events for different MC models when protons are tagged in AFP or not.

3.5 Medium luminosity measurements

Inclusive diffractive measurements

Medium luminosity measurements with the rapidity gap method used in Alice (two new scintillator hodoscopes covering $-7.0 < \eta < -4.9$ and $4.8 < \eta < 6.3$ are being installed in Alice in order to improve the forward coverage) or with proton tagging in AFP and CMS-TOTEM allow constraining

further the pomeron structure using γ+jet and dijet events [14]. The aim is to answer mainly the following questions that are fundamental from the QCD point of view:

- Is it the same object (the same pomeron) which explains diffraction in pp (LHC) and ep (HERA)? Are the measurements compatible between the different accelerators?
- If yes, what are the further constraints of the pomeron structure in terms of quarks and gluons?
- What is the value of the survival probability? It is important to measure it since it is difficult to compute it theoretically being sensitive to non-perturbative physics

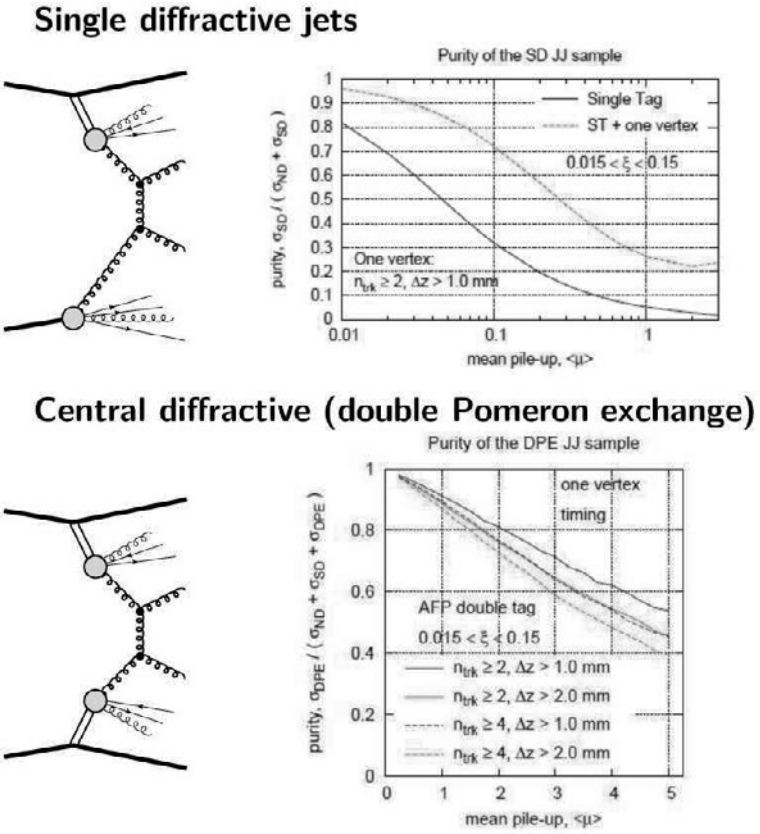

Figure 55: Feasibility studies of measuring jet production cross section in single diffractive and double pomeron exchange events.

Feasibility studies have been performed in ATLAS (and measurements started in CMS-TOTEM at 8 TeV) concerning the possibility to measure jet production cross sections in single diffractive and double pomeron exchange events at low β^*. The results are shown in Fig. 55 where the sample purity is shown as a function of pile up (the main background being due to non diffractive events superimposed by protons originating from soft diffractive events). In order to obtain a quite pure sample with a purity larger than 70%, low pile up runs ($\mu \sim$0.1) are needed for single diffractive jet measurements whereas moderate pile up ($\mu \sim 2-3$) is needed for double pomeron exchange jet measurements together with the request of the presence of a single reconstructed vertex. Typically, a few days of data taking will be enough to perform these measurements useful to constrain further the pomeron structure. It is also worth noticing that these measurements are also possible at higher values of β^*.

The CMS-TOTEM collaboration also studied many additional processes to be measured at high β^* [12]. For instance, 10 pb^{-1} of data are enough to obtain 3080 $\pm$ 90 single diffractive J/Ψ by tagging two muons of opposite charges with $3.05 < M_{\mu\mu} < 3.15$ GeV, 340$\pm$10 and 30$\pm$1 single diffractive W and Z by requesting a leading lepton with p_T >20 GeV.

Last but not least, the medium luminosity runs will allow probing the BFKL evolution using the jet gap jet events in diffraction [14].

Exclusive diffraction

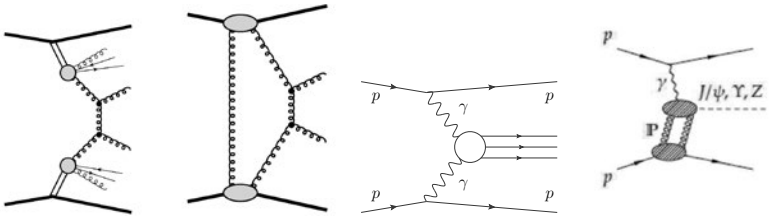

Figure 56: Exclusive diffractive and photon exchange processes. The left diagram shows the double pomeron exchange event for reference, the second one the QCD exclusive production, the third one the production of a system X via photon exchanges, and the last one the exclusive photo-production events.

The advantage of the exclusive diffractive and photon exchange processes illustrated in Fig. 56 is that all particles can be measured in the final state. Both protons can be measured in AFP or CMS-TOTEM and the produced particles (jets, vector mesons, Z boson....) in ATLAS or CMS, and there is no energy losses such as in the pomeron remnants as shown in Fig. 56, left diagram. It is thus possible to reconstruct the properties of the object produced exclusively (via photon and gluon exchanges) from the tagged proton since the system is completely constrained. It is worth mentioning that it is also possible to constrain the background by asking the matching between the information of the two protons and the produced object, and thus, central exclusive production is a potential channel for beyond standard modelphysics at high masses.

Exclusive vector mesons can be measured for instance in the LHCb experiment which recently measured for the first time the diffractive production of charmonium [15]. The Herschel scintillators are now being installed in LHCb to enhance the coverage at high rapidities in order to get a better control of non-exclusive background. Such channels are also sensitive to new physics: if a medium mass resonance due to a glueball or a tetraquark state exists, it could lead to a bump in the invariant mass distribution of the charmonium states.

The CMS-Totem experiment also performed extensive studies of possible measurements of exclusive states at high β^*. It is worth mentioning that the search for glueball states and the probe of the low x gluon density down to $x \sim 10^{-4}$ will be possible. With 1 pb^{-1}, it will be possible to confirm or not the existence of the unobserved possible $f_0(1710)$ and $f_0(1500)$ decay modes and with 5 to 10 pb^{-1}, the unambiguous spin determination and the precise measurement of cross-section times branching ratio. In addition, the measurement of the cross section times branching ratio for the three $\chi_{C,0,1,2}$ states, will be performed allowing a comparison with the results to the LHCb measurement [16] and the exclusive QCD calculations [17]

In addition, it is possible to measure the exclusive dijet production at the LHC with about 40 fb^{-1} and a pile up of 40 as was shown by the ATLAS and CT-PPS collaborations. Despite the high level of pile up background, it is possible to obtain a pure enough of exclusive jets that can further constrin the models of exclusive diffractive production.

4 Soft diffraction and measurement of the total cross section in ATLAS and TOTEM

4.1 The TOTEM experiment and the measurement of the total cross section

In this section, we will only give a short summary of the measurement of the total cross section by the TOTEM collaboration. For more details, see the proceedings written by U. Maor at this workshop [18].In Fig. 57, we display the different beam conditions (different values of β^*) that can be used to perform the total cross section as a function of t on the widest possible kinematical range. It is foreseen to perform the measurement at a β^* ∼1000 m in the next years at a center-of-mass energy of 13 TeV. The present result on the total, elastic and inelastic cross sections originating from TOTEM and ATLAS-ALFA experiments is given in Fig. 58 [19]. given in Fig. 58.

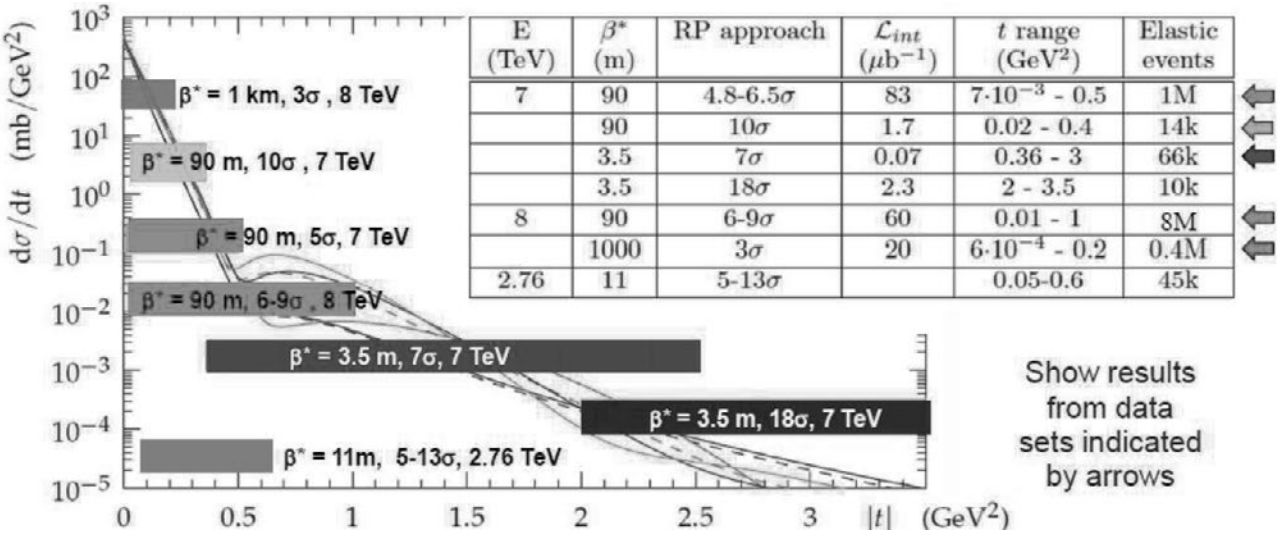

E (TeV)	β^* (m)	RP approach	$\mathcal{L}_{int}$ (μb^{-1})	t range (GeV^2)	Elastic events
7	90	4.8-6.5σ	83	$7{\cdot}10^{-3}$ - 0.5	1M
	90	10σ	1.7	0.02 - 0.4	14k
	3.5	7σ	0.07	0.36 - 3	66k
	3.5	18σ	2.3	2 - 3.5	10k
8	90	6-9σ	60	0.01 - 1	8M
	1000	3σ	20	$6{\cdot}10^{-4}$ - 0.2	0.4M
2.76	11	5-13σ		0.05-0.6	45k

Figure 57: Different beam conditions needed to measure the total cross section on a wide kinematical range in $|t|$.

4.2 Prospects in ATLAS/ALFA

The main motivation for installing the ALFA detectors is the total cross section measurement. The idea is to measure the elastic cross section in the Coulomb and interference region (see Fig. 2), which can be used to provide an absolute measurement of the luminosity. The elastic cross section is the sum of the coulombian, nuclear and interference terms

$$\frac{dN}{dt} = L\left(\frac{4\pi\alpha^2 G^4(t)}{|t|^2} - \frac{\alpha\rho\sigma_{tot}G^2(t)e^{-B|t|/2}}{|t|} + \frac{\sigma_{tot}^2(1+\rho)^2 e^{-B|t|}}{16\pi}\right). \tag{153}$$

The luminosity L, the total cross section, and the B and ρ parameters appearing in the elastic cross section formula are determined by fitting the dN/dt spectrum in the interference and nuclear regions. The measurement requires the possibility to detect the protons in the final state down to $t \sim 3.7\ 10^{-4}$ GeV^2 which means a proton angle down to 3 μrad, which requires special high β^* runs at low luminosity. The total uncertainties on the elastic cross section measurement are expected to be less than 3% (beam properties: 1.2%, detector properties: 1.4%, background substraction: 1.1% and a 1.8% statistical error for 100 hours of measurement at low luminosity).

The ALFA detector also allows to measure soft single diffractive events in dedicated runs where ALFA will be used to measure elastic events. It is possible to measure forward protons in the region:

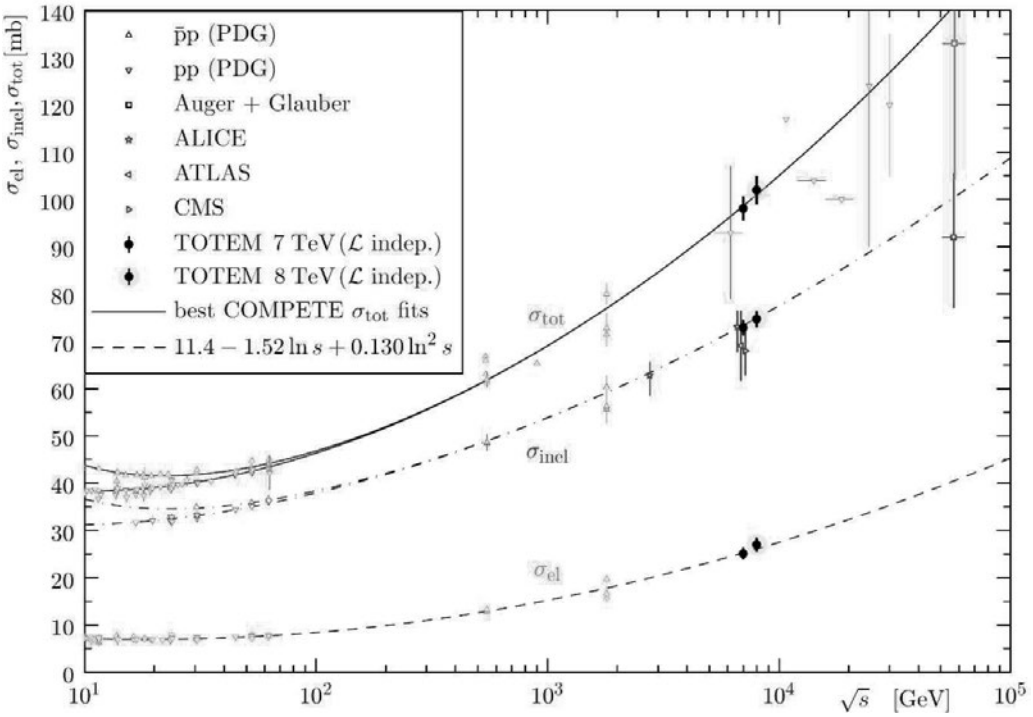

Figure 58: Measurement of the total, inelastic, and elastic cross sections by the TOTEM and ATLAS-ALFA collaborations.

$6.3 < E_{proton} < 7$ TeV, and single diffractive measurements are possible for $\xi < 0.01$ and non-diffractive proton measurements for $0.01 < \xi < 0.1$. 1.5 million events are expected in 100 hours at 10^{27} cm^{-2}s^{-1}.

5 Photon induced processes at the LHC and anomalous coupling studies

In this section, we discuss some potential measurements to be performed using proton tagging detectors at the LHC based on γ-induced processes. The main motivation is to explore rare events, searching for beyond standard model physics such as quartic anomalous couplings between photons and W/Z bosons and photons. We assume in the following intact protons to be tagged in dedicated detectors located at about 210 m for ATLAS (220 m for CMS).

In the first part of this section, we discuss the SM production of W and γ pairs at the LHC via photon exchanges. In the second, third and fourth sections, we discuss the sensitivities of these processes to trilinear and quartic gauge anomalous couplings.

5.1 Standard Model exclusive $\gamma\gamma$, WW and ZZ production

Standard Model exclusive $\gamma\gamma$ production at the LHC: Photon and gluon induced processes

In Fig. 60 and 61, we show the leading processes leading to two photons and two intact protons in the final state as an example. The first diagram (Fig. 60) corresponds to exclusive QCD diphoton production via gluon exchanges (the second gluon ensures that the exchange is colorless leading to intact protons in the final state) and the second one (Fig. 61) via photon exchanges, It is worth noticing that quark, lepton and W loops need to be considered in order to get the correct SM cross section for diphoton production as shown in Fig 62. The QCD induced processes from the Khoze Martin Ryskin model are dominant at low masses whereas the photon induced ones (QED processes) dominate at

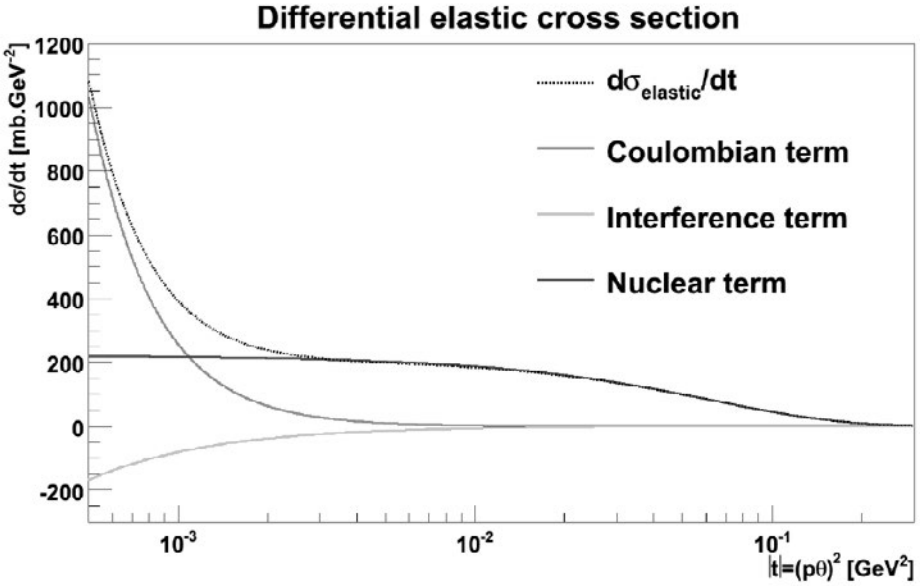

Figure 59: Coulombian, nuclear and interference terms in the elastic cross section.

higher diphoton masses [17]. It is very important to notice that the W loop contribution dominates at high diphoton masses [20–22] whereas this contribution is omitted in most studies. This is the first time that we put all terms inside a MC generator, FPMC [23].

Standard Model WW and ZZ production

In the Standard Model (SM) of particle physics, the couplings of fermions and gauge bosons are constrained by the gauge symmetries of the Lagrangian. The measurement of W and Z boson pair productions via the exchange of two photons allows to provide directly stringent tests of one of the most important and least understood mechanism in particle physics, namely the electroweak symmetry breaking.

The process that we study is the W pair production induced by the exchange of two photons [24]. It is a pure QED process in which the decay products of the W bosons are measured in the central detector and the scattered protons leave intact in the beam pipe at very small angles and are detected in AFP or CT-PPS. All these processes as well as theb different diffractive backgrounds were inplemented in the FPMC Monte Carlo [23].

After simple cuts to select exclusive W pairs decaying into leptons, such as a cut on the proton momentum loss of the proton ($0.0015 < \xi < 0.15$) — we assume the protons to be tagged in AFP or CT-PPS at 210 and 420 m — on the transverse momentum of the leading and second leading leptons at 25 and 10 GeV respectively, on $\not{E}_T > 20$ GeV, $\Delta\phi > 2.7$ between leading leptons, and $160 < W < 500$ GeV, the diffractive mass reconstructed using the forward detectors, the background is found to be less than 1.7 event for 30 fb^{-1} for a SM signal of 51 events [24].

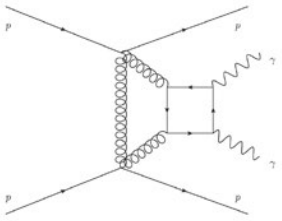

Figure 60: Diphoton QCD exclusive production.

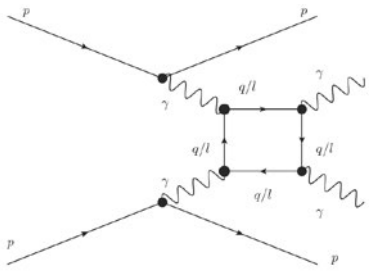

Figure 61: Diphoton production via photon exchanges.

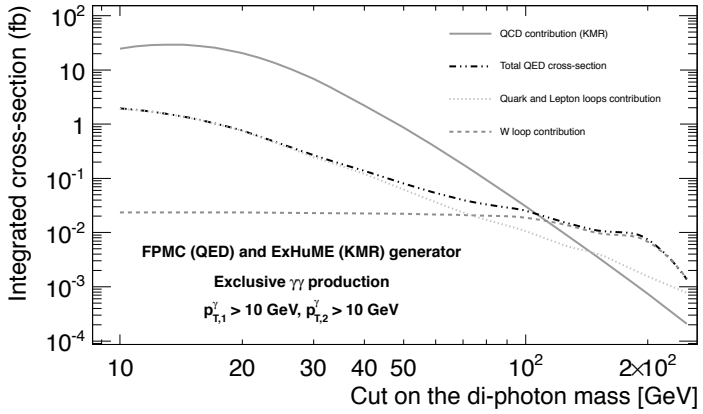

Figure 62: Diphoton production cross section as a function of the diphoton mass requesting two intact protons in the final state and the photons to have a transverse momentum larger than 10 GeV. The QCD exclusive processes (Khoze Martin Ryskin) in full line dominate at low masses while QED diphoton production dominates at higher masses (dashed lines). The QED production corresponds to diphoton production via lepton/fermion loops (dotted line) and W boson loops (dashed-dotted line).

5.2 Triple anomalous gauge couplings

In Ref. [25], we also studied the sensitivity to triple gauge anomalous couplings at the LHC. The Lagrangian including anomalous triple gauge couplings λ^γ and $\Delta\kappa^\gamma$ is the following

$$\begin{aligned}\mathcal{L} \sim\ & (W^\dagger_{\mu\nu}W^\mu A^\nu - W_{\mu\nu}W^{\dagger\mu}A^\nu) \\ & +(1+\Delta\kappa^\gamma)W^\dagger_\mu W_\nu A^{\mu\nu} + \frac{\lambda^\gamma}{M_W^2}W^\dagger_{\rho\mu}W^\mu{}_\nu A^{\nu\rho}). \end{aligned} \quad (154)$$

The strategy is the same as for the SM coupling studies: we first implement this lagrangian in FPMC [23] and we select the signal events when the Z and W bosons decay into leptons. The difference is that the signal appears at high mass for λ^γ and $\Delta\kappa^\gamma$ only modifies the normalization and the low mass events have to be retained. The sensitivity on triple gauge anomalous couplings is a gain of about a factor 3 with respect to the LEP limits, which represents one of the best reaches before the LHC.

5.3 Quartic WW and ZZ anomalous couplings

The parameterization of the quartic couplings based on [26] is adopted. The cuts to select quartic anomalous gauge coupling WW events are similar as the ones we mentioned in the previous section, namely $0.0015 < \xi < 0.15$ for the tagged protons corresponding to the AFP or CT-PPS detector

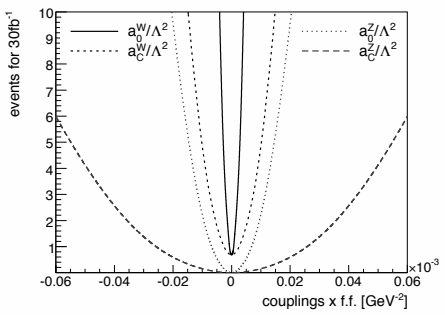

Figure 63: Number of events for signal due to different values of anomalous couplings after all cuts (see text) for a luminosity of 30 fb^{-1}.

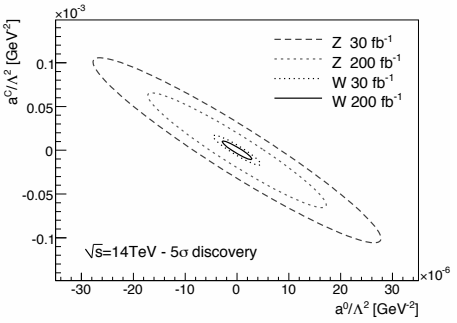

Figure 64: 5σ discovery contours for all the WW and ZZ quartic couplings at $\sqrt{s} = 14$ TeV for a luminosity of 30 fb^{-1} and 200 fb^{-1}.

at 210 and 420 m, $\not{E}_T > 20$ GeV, $\Delta\phi < 3.13$ between the two leptons. In addition, a cut on the p_T of the leading lepton $p_T > 160$ GeV and on the diffractive mass $W > 800$ GeV are requested since anomalous coupling events appear at high mass. After these requirements, we expect about 0.7 background events for an expected signal of 17 events if the anomalous coupling is about four orders of magnitude lower than the present LEP limit [27] ($|a_0^W/\Lambda^2| = 5.4\ 10^{-6}$) or two orders of magnitude lower with respect to the D0 and CDF limits [28] for a luminosity of 30 fb^{-1}. The strategy to select anomalous coupling ZZ events is analogous and the presence of three leptons or two like sign leptons are requested. Table 1 gives the reach on anomalous couplings at the LHC for luminosities of 30 and 200 fb^{-1} compared to the present OPAL limits from the LEP accelerator [27]. More recent limits were published recently by the D0 and CMS collaborations [28] on a_0^W and a_C^W, and they are respectively 1.5 10^{-4} and 5 10^{-4} from CMS with a form factor of 500 GeV,

Figs. 63 and 64 show respectively the number of expected events for signal as a function of the anomalous coupling value and the 5σ discovery contours for all WW and ZZ anomalous couplings for 30 and 200 fb^{-1}. It is possible to reach the values expected in extra dimension models. The tagging of the protons using the ATLAS Forward Physics detectors is the only method at present to test so small values of quartic anomalous couplings.

Couplings	OPAL limits	Sensitivity @ $\mathcal{L} = 30$ (200) fb^{-1}	
	[GeV^{-2}]	5σ	95% CL
a_0^W/Λ^2	[-0.020, 0.020]	5.4 10^{-6} (2.7 10^{-6})	2.6 10^{-6} (1.4 10^{-6})
a_C^W/Λ^2	[-0.052, 0.037]	2.0 10^{-5} (9.6 10^{-6})	9.4 10^{-6} (5.2 10^{-6})
a_0^Z/Λ^2	[-0.007, 0.023]	1.4 10^{-5} (5.5 10^{-6})	6.4 10^{-6} (2.5 10^{-6})
a_C^Z/Λ^2	[-0.029, 0.029]	5.2 10^{-5} (2.0 10^{-5})	2.4 10^{-5} (9.2 10^{-6})

Table 18: Reach on anomalous couplings obtained in γ induced processes after tagging the protons in AFP or CT-PPS compared to the present OPAL limits. The 5σ discovery and 95% C.L. limits are given for a luminosity of 30 and 200 fb^{-1} [24]

The search for quartic anomalous couplings between γ and W bosons was performed again after

a full simulation of the ATLAS detector including pile up [29] assuming the protons to be tagged in AFP or CT-PPS at 210 m only. Integrated luminosities of 40 and 300 fb^{-1} with, respectively, 23 or 46 average pile-up events per beam crossing have been considered. In order to reduce the background, each W is assumed to decay leptonically (note that the semi-leptonic case in under study). The full list of background processes used for the ATLAS measurement of Standard Model WW cross-section was simulated, namely $t\bar{t}$, WW, WZ, ZZ, W+jets, Drell-Yan and single top events. In addition, the additional diffractive backgrounds mentioned in the previous paragraph were also simulated, The requirement of the presence of at least one proton on each side of AFP or CT-PPS within a time window of 10 ps allows us to reduce the background by a factor of about 200 (50) for $\mu = 23$ (46). The p_T of the leading lepton originating from the leptonic decay of the W bosons is required to be $p_T >$ 150 GeV, and that of the next-to-leading lepton $p_T > 20$ GeV. Additional requirement of the dilepton mass to be above 300 GeV allows us to remove most of the diboson events. Since only leptonic decays of the W bosons are considered, we require in addition less than 3 tracks associated to the primary vertex, which allows us to reject a large fraction of the non-diffractive backgrounds (e.g. $t\bar{t}$, diboson productions, W+jet, etc.) since they show much higher track multiplicities. Remaining Drell-Yan and QED backgrounds are suppressed by requiring the difference in azimuthal angle between the two leptons $\Delta\phi < 3.1$. After these requirements, a similar sensitivity with respect to fast simulation without pile-up was obtained.

5.4 Quartic photon anomalous couplings

Theoretical motivations

In this section, four-photon (4γ) interactions through diphoton production via photon fusion with intact outgoing protons are considered. In the assumption of a new physics mass scale Λ heavier than experimentally accessible energy E, all new physics manifestations can be described using an effective Lagrangian valid for $\Lambda \gg E$. Among these operators, the pure photon dimension-eight operators

$$\mathcal{L}_{4\gamma} = \zeta_1^\gamma F_{\mu\nu} F^{\mu\nu} F_{\rho\sigma} F^{\rho\sigma} + \zeta_2^\gamma F_{\mu\nu} F^{\nu\rho} F_{\rho\lambda} F^{\lambda\mu} \tag{155}$$

can induce the $\gamma\gamma\gamma\gamma$ process, highly suppressed in the SM [20, 30]. We discuss here possible new physics contributions to $\zeta_{1,2}^\gamma$ that can be probed and discovered at the LHC using the forward proton detectors.

Loops of heavy charged particles contribute to the 4γ couplings [20, 30] as $\zeta_i^\gamma = \alpha_{\rm em}^2 Q^4 m^{-4} N c_{i,s}$, where $c_{1,s}$ is related to the spin of the heavy particle of mass m running in the loop and Q its electric charge. The factor N counts all additional multiplicities such as color or flavor. These couplings scale as $\sim Q^4$ and are enhanced in presence of particles with large charges. For example, certain light composite fermions, characteristic of composite Higgs models, have typically electric charges of several units. For a 500 Gev vector (fermion) resonance with $Q = 3$ (4), large couplings ζ_i^γ of the order of $10^{-13} - 10^{-14}$ Gev^{-4} can be reached.

Beyond perturbative contributions to ζ_i^γ from charged particles, non-renormalizable interactions of neutral particles are also present in common extensions of the SM. Such theories can contain scalar, pseudo-scalar and spin-2 resonances that couple to the photon and generate the 4γ couplings by tree-level exchange as $\zeta_i^\gamma = (f_s\, m)^{-2}\, d_{i,s}$, where $d_{1,s}$ is related to the spin of the particle. Strongly-coupled conformal extensions of the SM contain a scalar particle ($s = 0^+$), the dilaton. Even a 2 TeV dilaton can produce a sizable effective photon interaction, $\zeta_1^\gamma \sim 10^{-13}$ GeV^{-4}. These features are reproduced at large number of colors by the gauge-gravity correspondence in a warped extra dimension. Warped-extra dimensions also feature Kaluza-Klein (KK) gravitons [31], that can induce anomalous couplings [30]

$$\zeta_i^\gamma = \frac{\kappa^2}{8\tilde{k}^4}\, d_{i,2}\,, \tag{156}$$

where $\tilde{k}$ is the IR scale that determines the first KK graviton mass and κ is a parameter that can be taken $\mathcal{O}(1)$. For $\kappa \sim 1$, and $m_2 \lesssim 6$ TeV, the photon vertex can easily exceed $\zeta_2^\gamma \sim 10^{-14}$ GeV^{-4}.

Experimental sensitivity to quartic four photon couplings

As we mentionned already, the $\gamma\gamma\gamma\gamma$ process (Fig. 61) can be probed via the detection of two intact protons in the forward proton detectors and two energetic photons in the corresponding electromagnetic calorimeters [20]. The SM cross section of diphoton production with intact protons is dominated by the QED process at high diphoton mass — and not by gluon exchanges — and is thus very well known.

As mentioned in Ref. [32], the photon identification efficiency is expected to be around 75% for $p_T > 100$ GeV, with jet rejection factors exceeding 4000 even at high pile-up (>100). In addition, about 1% of the electrons are mis-identified as photons. These numbers are used in the phenomenological study presented below.

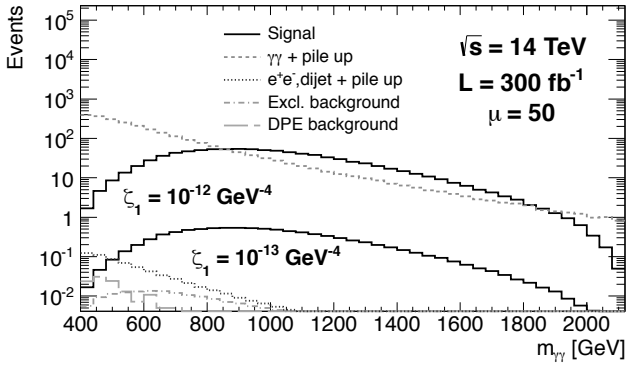

Figure 65: Diphoton invariant mass distribution for the signal ($\zeta_1 = 10^{-12},\ 10^{-13}$ Gev^{-4}, see Eq. 155) and for the backgrounds (dominated by $\gamma\gamma$ with protons from pile-up), requesting two protons in the forward detectors and two photons of $p_T > 50$ GeV with at least one converted photon in the central detector, for a luminosity of 300 fb^{-1} and an average pile-up of $\mu = 50$.

Cut / Process	Signal (full)	Signal with (without) f.f (EFT)	Excl.	DPE	DY, di-jet + pile up	$\gamma\gamma$ + pile up
$[0.015 < \xi_{1,2} < 0.15,$ $p_{\mathrm{T1,(2)}} > 200, (100)$ GeV]	130.8	36.9 (373.9)	0.25	0.2	1.6	2968
$m_{\gamma\gamma} > 600$ GeV	128.3	34.9 (371.6)	0.20	0	0.2	1023
$[p_{\mathrm{T2}}/p_{\mathrm{T1}} > 0.95,$ $\lvert\Delta\phi\rvert > \pi - 0.01]$	128.3	34.9 (371.4)	0.19	0	0	80.2
$\sqrt{\xi_1\xi_2 s} = m_{\gamma\gamma} \pm 3\%$	122.0	32.9 (350.2)	0.18	0	0	2.8
$\lvert y_{\gamma\gamma} - y_{pp}\rvert < 0.03$	119.1	31.8 (338.5)	0.18	0	0	0

Table 19: Number of signal events for $S = 1$, $Q_{\mathrm{eff}} = 4$, $m = 340$ GeV and background events after various selections for an integrated luminosity of 300 fb^{-1} and $\mu = 50$ at $\sqrt{s} = 14$ TeV. Values obtained using the corresponding EFT couplings with and without form factors are also displayed. At least one converted photon is required. Excl. stands for exclusive backgrounds and DPE for double pomeron exchange backgrounds (see text).

As for the previous studies, the anomalous $\gamma\gamma\gamma\gamma$ process has been implemented in the Forward

Physics Monte Carlo (FPMC) generator [23]. The FPMC generator was also used to simulate the background processes giving rise to two intact protons accompanied by two photons, electrons or jets that can mimic the photon signal. Those include exclusive SM production of $\gamma\gamma\gamma\gamma$ via lepton and quark boxes and $\gamma\gamma \to e^+e^-$. The central exclusive production of $\gamma\gamma$ via two-gluon exchange, not present in FPMC, was simulated using ExHuME [33]. This series of backgrounds is called "Exclusive" in Table 19 and Figs. 65, 66. FPMC was also used to produce $\gamma\gamma$, Higgs to $\gamma\gamma$ and dijet productions via double pomeron exchange (called DPE background in Table 19 and Fig. 65). Such backgrounds tend to be softer than the signal and can be suppressed with requirements on the transverse momenta of the photons and the diphoton invariant mass. In addition, the final-state photons of the signal are typically back-to-back and have about the same transverse momenta. Requiring a large azimuthal angle $|\Delta\phi| > \pi - 0.01$ between the two photons and a ratio $p_{T,2}/p_{T,1} > 0.95$ greatly reduces the contribution of non-exclusive processes.

Additional background processes include the quark and gluon-initiated production of two photons, two jets and Drell-Yan processes leading to two electrons. The two intact protons arise from pile-up interactions (these backgrounds are called $\gamma\gamma$ + pile-up and e^+e^-, dijet + pile-up in Table 19).These events were produced using HERWIG [34] and PYTHIA [35]. The pile-up background is further suppressed by requiring the proton missing invariant mass to match the diphoton invariant mass within the expected resolution and the diphoton system rapidity and the rapidity of the two protons to be similar.

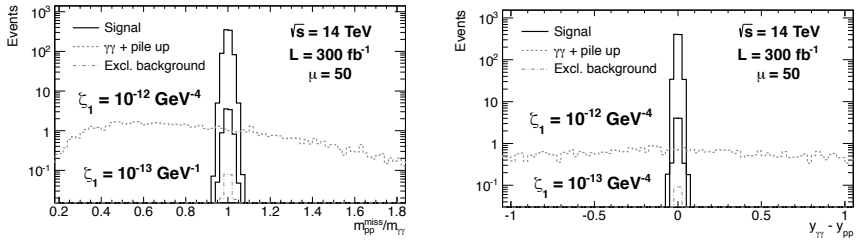

Figure 66: Diphoton to missing proton mass ratio (left) and rapidity difference (right) distributions for signal considering two different coupling values (10^{-12} and 10^{-13} GeV^{-4}, see Eq. 155) and for backgrounds after requirements on photon p_T, diphoton invariant mass, p_T ratio between the two photons and on the angle between the two photons. At least one converted photon is required. The integrated luminosity is 300 fb^{-1} and the average pile-up is $\mu = 50$.

The number of expected signal and background events passing respective selections is shown in Table 19 for an integrated luminosity of 300 fb^{-1} for a center-of-mass energy of 14 TeV [20]. Exploiting the full event kinematics with the forward proton detectors allows to completely suppress the background with a signal selection efficiency after the acceptance cuts exceeding 70%. Tagging the protons is absolutely needed to suppress the $\gamma\gamma$ + pile-up events. Further background reduction is even possible by requiring the photons and the protons to originate from the same vertex that provides an additional rejection factor of 40 for 50 pile-up interactions, showing the large margin on the background suppression. A similar study at a higher pile-up of 200 was performed and led to a very small background. The sensitivities on photon quartic anomalous couplings are given in Table 20. The sensitivity extends up to $7 \cdot 10^{-15}$ GeV^{-4} allowing us to probe further the models of new physics described above.

If discovered at the LHC, $\gamma\gamma\gamma\gamma$ quartic anomalous couplings would be a major discovery related to the existence of extra dimensions in the universe asa an example. In addition, it might be inveestigated if there could be a link with some experiments in atomic physics. As an example, the Aspect photon correlation experiments [36] might be interpreted via the existence of extra dimensions. Photons could communicate through extra dimensions and the deterministic interpretation of Einstein for these experiments might be true if such anomalous couplings exist. From the point of view of atomic

Luminosity	300 fb^{-1}	300 fb^{-1}	300 fb^{-1}	300 fb^{-1}	3000 fb^{-1}
pile up (μ)	50	50	50	50	200
coupling (GeV^{-4})	≥ 1 conv. γ $5\,\sigma$	≥ 1 conv. γ 95% CL	all γ $5\,\sigma$	all γ 95% CL	all γ 95% CL
ζ_1 f.f.	$8 \cdot 10^{-14}$	$5 \cdot 10^{-14}$	$4.5 \cdot 10^{-14}$	$3 \cdot 10^{-14}$	$2.5 \cdot 10^{-14}$
ζ_1 no f.f.	$2.5 \cdot 10^{-14}$	$1.5 \cdot 10^{-14}$	$1.5 \cdot 10^{-14}$	$9 \cdot 10^{-15}$	$7 \cdot 10^{-15}$
ζ_2 f.f.	$2 \cdot 10^{-13}$	$1 \cdot 10^{-13}$	$9 \cdot 10^{-14}$	$6 \cdot 10^{-14}$	$4.5 \cdot 10^{-14}$
ζ_2 no f.f.	$5 \cdot 10^{-14}$	$4 \cdot 10^{-14}$	$3 \cdot 10^{-14}$	$2 \cdot 10^{-14}$	$1.5 \cdot 10^{-14}$

Table 20: $5\,\sigma$ discovery and 95% CL exclusion limits on ζ_1 and ζ_2 couplings in GeV^{-4} (see Eq. 155) with and without form factor (f.f.), requesting at least one converted photon (≥ 1 conv. γ) or not (all γ). All sensitivities are given for 300 fb^{-1} and $\mu = 50$ pile up events (medium luminosity LHC) except for the numbers of the last column which are given for 3000 fb^{-1} and $\mu = 200$ pile up events (high luminosity LHC).

physics, the results of the Aspect experiments would depend on the distance of the two photon sources. Further more, it is clear that extra dimensions might be relevant also for the fast expansion of the universe within inflation models.

5.5 Conclusion

In this section, we detailled the interest of tagging the intact protons to study in detail WW, ZZ and $\gamma\gamma$ productions via photon exchanges. Uprecedented sensitivities can be achieved at the LHC in the CMS-TOTEM and ATLAS experiments on quartic anomalous couplings, especially on $\gamma\gamma\gamma\gamma$ couplings, that will lead to one of the best sensitivity on extra dimensions at the LHC.

6 The installation of forward proton detectors in CMS and ATLAS

6.1 The AFP and CT-PPS projects

Several improvements are made to the ATLAS and CMS detectors to exploit the new energy regime of 13 TeV at the LHC; this section describes the project to install the ATLAS Forward Proton (AFP) detector at 206 and 214 meters on both sides of the ATLAS experiment [29] (see Fig. 67) and the similar project by the TOTEM and CMS collaborations, the so called CT-PPS, to be installed on both sides of the CMS detector. In this article, we will concentrate on the main characteristics of the AFP and CT-PPS detectors, while their physics reach was described in the previous section [20, 24, 25].

Each arm of the AFP detector will consist of two sections: AFP1 at 206 meters, and AFP2, at 220 meters. In AFP1, a tracking station composed by 6 layers of Silicon detectors will be deployed. The second section, AFP2, will contain a second identical tracking station and a timing detector. In addition, a similar structure could be installed at about 420 m from the ATLAS interaction point. The aim of the combined two arms of this setup is to tag the protons emerging intact from the pp interactions, allowing ATLAS to exploit the program of diffractive and photon induced processes described in the previous sections. Likewise, the CT-PPS of CMS will also use the same combination of tracking and timing detectors, with the far station using specially designed cylindrical roman pots to house the timing detectors.

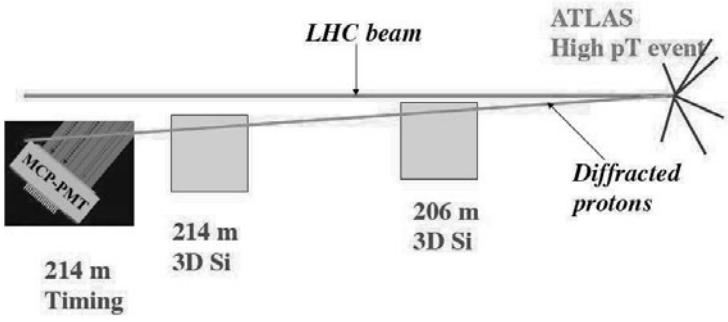

Figure 67: Scheme of the AFP proton detector in ATLAS. The same detector is implemented on the other side of ATLAS.

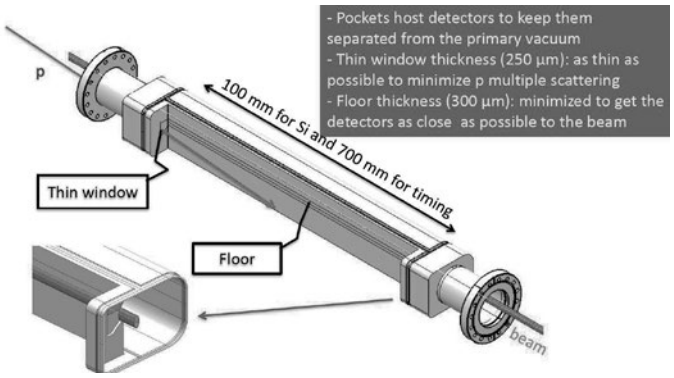

Figure 68: Scheme of the movable beam pipe.

6.2 Movable beam pipes and roman pots

In order to house the detectors needed by the AFP and CT-PPS projects, two different types of modification of the beam-pipe are currently considered: (i) roman pots and (ii) movable beam pipes). Roman pots have been used already in many experiments at the SPS, HERA, Tevatron and LHC colliders (in the TOTEM and ATLAS-ALFA experiments). The roman pots, in their basic design, are pockets where the detectors can be hosted. These pockets are pushed inside the beam pipe to a position closer to the beam line once stable beam has been declared (a typical motion is of the order of a few cm). To minimize multiple scattering, protons will enter the roman pots via a thin window located at the bottom of the pot, on the side facing the beams. Different types of roman pots can host the tracking and timing detectors: tracking detectors need less space than timing detectors, and therefore can be housed in smaller roman pots.

Conversely, in the movable beam pipe design, no pocket is pushed closer to the beam, but the whole beam pipe moves closer to the beam. The idea of movable Hamburg beam pipes is quite simple [37]: a section of the LHC beam pipe is replaced by a larger one, specially designed to have a cutout to host the detectors. When allowed by beam conditions, using specially designed bellows that allow for transverse motions, this part of the beam pipe is moved, by about 2.5 cm, so that the detectors located at its edge (called pocket) are brought closer to the beam. In its design, the most challenging aspect is the minimization of the thickness of the portions called floor and window (see Fig. 68). This is necessary as the floor might be rather long, of the order of 10-40 centimeters in the direction parallel to the motion of the particles: minimizing its depth of the floor ensures that the detectors can be brought as close to the beam as possible allowing detecting protons scattered at very small angles. Two configurations exist for the movable beam pipes: the first one at 206 m from the ATLAS interaction point hosts a Si detector (floor length of about 100 mm) and the second one (floor length

of about 400 mm) the timing and the Si detectors.

The AFP and CT-PPS detectors will use Roman Pots in their starting configuration. In the meantime, the development of the Hamburg beam pipe is carried on together by both collaborations. However, it is clear that movable beam pipes are needed at 420 m, if later upgrades include installation of forward detectors at that location. At 420 m, not enough space is available and new specially designed cryostats have been developed to host these movable beam pipes in the cold region. The usage of roman pots at 420 m would require a costly cryogenic bypass to be installed to isolate the part of the beam pipe where roman pots would be installed.

6.3 3D Silicon detectors

The purpose of the tracker system is to measure points along the trajectory of beam protons that are deflected at small angles as a result of collisions. The tracker, when combined with the LHC dipole and quadrupole magnets, forms a powerful momentum spectrometer. Silicon tracker stations will be installed in Hamburg beam pipes or roman pots at ± 206 and ± 214 m from the ATLAS interaction point (and also at 420 m later if these additional detectors are appoved).

The key requirements for the silicon tracking system at 220 m are:

- Spatial resolution of $\sim$ 10 (30) μm per detector station in x (y)
- Angular resolution for a pair of detectors of a few μrad
- High efficiency over the area of 20 mm $\times$ 20 mm corresponding to the distribution of diffracted protons
- Minimal dead space at the edge of the sensors towards the beam line, allowing measuring the scattered protons at low angles
- Sufficient radiation hardness in order to sustain the radiation at high luminosity
- Capable of robust and reliable operation at high LHC luminosity

The basic building unit of the AFP detection system is a module consisting of an assembly of a sensor array, on-sensor read-out chip(s), electrical services, data acquisition and detector control system. The module will be mounted on the mechanical support with embedded cooling and other necessary services. The sensors are double sided 3D 50×250 micron pixel detectors with slim-edge dicing built by FBK and CNM companies. The sensor efficiency has been measured to be close to 100% over the full size in beam tests. A possible upgrade of this device will be to use 3D edgeless Silicon detectors built in a collaboration between SLAC, Manchester, Oslo, Bergen...

A new front-end chip FE-I4 has been developed for the Si detector by the Insertable B Layer (IBL) collaboration in ATLAS [38]. The FE-I4 integrated circuit contains readout circuitry for 26 880 hybrid pixels arranged in 80 columns on 250 μm pitch by 336 rows on 50 μm pitch, and covers an area of about 19 mm $\times$ 20 mm. It is designed in a 130 nm feature size bulk CMOS process. Sensors must be DC coupled to FE-I4 with negative charge collection. The FE-I4 is very well suited to the AFP requirements: the granularity of cells provides a sufficient spatial resolution, the chip is radiation hard enough up to a dose of 3 MGy, and the size of the chip is sufficiently large that one module can be served by just one chip.

The dimensions of the individual cells in the FE-I4 chip are 50 μm $\times$ 250 μm in the x and y directions, respectively. Therefore to achieve the required position resolution in the x-direction of $\sim$ 10 μm, six layers with sensors are required (this gives $50/\sqrt{12}/\sqrt{5} \sim 7$ μm in x and roughly 5 times worse in y). Offsetting planes alternately to the left and right by one half pixel will give a further reduction in resolution of at least 30%. The AFP sensors are expected to be exposed to a dose of 30 kGy per year at the full LHC luminosity of $10^{34}\text{cm}^{-2}\text{s}^{-1}$.

The baseline CT-PPS tracking system is also based on 3D pixel sensors, produced either by FBK (Trento, Italy) or CNM (Barcelona, Spain), which provide the best performance in terms of active region and radiation hardness.

The chosen configuration for the tracking system consists of two detector stations in each arm. Each station will contain one stack of silicon tracking detectors. Each stack will consist of six planes, where each plane conatains a 1.6 $\times$ 2.4 cm^2 pixel sensor read out by six PSI46dig readout chips ROCs [39]. Each ROC reads 52 $\times$ 80 pixels with dimensions 150 $\times$ 100 μm^2. The design of the front-end electronics and of the DAQ is based on that developed for the Phse I upgrade of the CMS silicon pixel detectors [40].

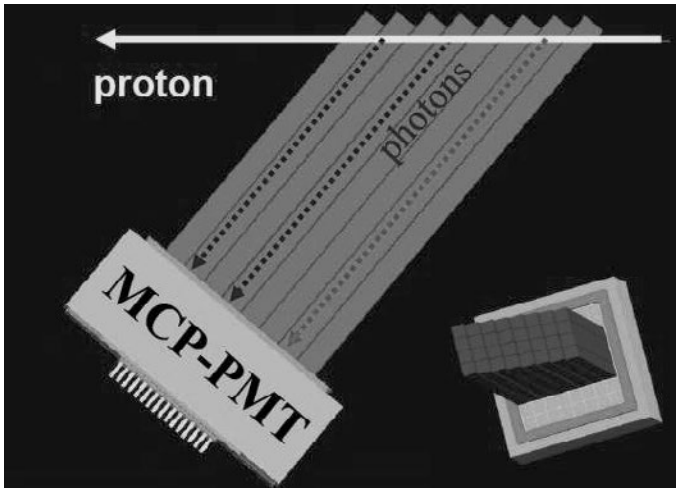

Figure 69: A schematic diagram of the QUARTIC fast timing detector.

6.4 Timing detectors

Requirements and present achievement

A fast timing system that can precisely measure the time difference between the two outgoing scattered protons is a key component of the AFP and CT-PPS detectors. The time difference is equivalent to a constraint on the event vertex, thus the AFP and CT-PPS timing detectors can be used to reject overlapping background events by establishing that the two scattered protons did not originate from the same vertex that triggered the central ATLAS or CMS detectors. The final timing system should have the following characteristics [41]:

- 10 ps or better resolution (which leads to a factor 40 rejection on pile up background)
- Efficiency close to 100% over the full detector coverage
- High rate capability (there is a bunch crossing every 25 ns at the nominal LHC)
- Enough segmentation for multi-proton timing
- High level trigger capability

Fig. 69 shows a schematic overview of the first proposed timing system in AFP, consisting of a quartz-based Cerenkov detector coupled to a microchannel plate photomultiplier tube (MCP-PMT), followed by the electronic elements that amplify, measure, and record the time of the event along with a stabilized reference clock signal. The QUARTIC detector consists of an array of 8×4 fused silica bars ranging in length from about 8 to 12 cm and oriented at the average Cerenkov angle. A proton that is sufficiently deflected from the beam axis will pass through a row of eight bars emitting

Cerenkov photons providing an overall time resolution that is approximately $\sqrt{8}$ times smaller than the single bar resolution of about 30 ps, thus approaching the 10 ps resolution goal. Prototype tests have generally been performed on one row (8 channels) of 5 mm $\times$ 5 mm pixels, while the initial detector is foreseen to have four rows to obtain full acceptance out to 20 mm from the beam. The beam tests lead to a time resolution per bar of the order of 34 ps. The upgraded design of the timing detector has equal rate pixels, and we plan to reduce the width of detector bins close to the beam, where the proton density is highest.

The CT-PPS also has a detector based on Cerenkov technology as the baseline proposal. It has chosen a Cherenkov L-bar Quartic design (Quartz Timing Cherenkov) with 5 $\times$ 4 equal to twenty 3 $\times$ 3 mm^2 independent channels. They are read-out by SiPM photodetectors, relatively far from the beam, in a region where the neutron flux is $\sim$2 10^{12} neq/cm^2 per 100 fb^{-1}. SiPM devices that tolerate this radiation level are available, and already in use in the CMS detector [42]. The SiPMs will probably require replacement after 100 fb^{-1}, which is feasible given the small number of devides involved. Two such Quartic detectors fit inside a cylindrical roman pot, providing a combined resolution of the order of 20 ps.

Future developments

At higher luminosity of the LHC (phase I starting in 2019), higher pixelisation of the timing detector will be required in order to fight against high pile up environment. For this sake, a R&D phase to develop timing detector developments based on Silicon sensors [11], and diamonds [43] has started. This new R&D aims at installing a prototype of such detector at the LHC in the TOTEM experiment as soon as they are available. In parallel to this sensor R&D, a new timing readout chip has been developed in Orsay/Saclay. It uses waveform sampling to reach the best possible timing resolution and it is described in detail in the next section.

The CT-PPS project has now been endorsed by the CMS and TOTEM collaboration at least for the first phase at low luminosity. If everythings works as expected, and the beam induced background (not easily simulated) is not found to be an issue at 14 TeV, the project will be naturally approved to work at higher luminosity. The AFP project is almost at the same stage, pending the approval at low luminosities until enough resources are found within and outside the ATLAS collaboration.

6.5 Timing detector optimisation for pile up rejection

In this section, we discuss possible optimisation of the timing detector in terms of spacial resolution in order to reject pile up background.

Proton detection in the forward region

The main source of background in the timing detectors is due to pile up events. Intact protons may obviously originate from the diffractive and photon-exchange events but also from additional soft interactions (pile up). For instance a non-diffractive WW event can be superimposed with two single diffractive soft events with intact porons and it is important to be able to distinguish this background from the event where both protons originate from the WW vertex. In order to suppress this background, it is useful to measure precisely the proton time-of-flights in order to know if the protons originate from the main event hard vertex or not.

Two parameters to build a detector are important to reject pile up:

- the precision of the proton time-of-flight, which is the timing detector resolution. Typically a measurement of 10 ps gives a precision of 2.1 mm on the vertex position
- the pixelisation of the timing detector: at highest luminosity, the number of intact protons per bunch crossing is high and in order to compute the time-of-flight of each proton it is needed

to have enough pixelisation or space resolution so that each proton can be detected in different cells of the timing detector. If two protons with different time-of-flight fall in the same cell, the information is lost.

Pixelisation of the timing detector

In order to study the required pixelisation of the timing detector, we simulated 10 million minimum bias events (non diffractive, single diffractive and double diffractive events) using the PYTHIA generator. The protons were transported through the LHC magnets up to the proton detectors. Events are characterised as no tagged (NT), single tagged (ST) and double tagged (DT) depending on the number of protons in the forward proton detector acceptance. For one minimim bias event, we get a probability of 97% NT, p =1.6% ST, and q =0.01% DT. The multinomial distribution was adopted to simulate pile up since we assume that the different interactions are independant [44]. For a given number of pile up proton N, the probability to have N_L (N_R) protons tagged in the left (right) side only, N_B protons on both sides and N_N protons not tagged reads:

$$P(N_B, N_L, N_R, N_N) = \frac{N!}{N_B! N_L! N_R! N_N!} p^{N_L} q^{N_B} p^{N_R} (1-2p-q)^{N_N} \tag{157}$$

and the probability of no proton tagged, of at least one proton tagged on the left side, and of at least one proton tagged on both sides reads

$$P_{no\ hit} = P(0,0,0,N) = (1-2p-q)^N \tag{158}$$

$$P_{hit\ left} = \sum_{N_L=1}^{N} P(0, N_L, 0, N-N_L) = (1-p-q)^N - (1-2p-q)^N \tag{159}$$

$$P_{double\ hit} = 1 - P_{no\ hit} - 2P_{hit\ left} = 1 + (1-2p-q)^N - 2(1-p-q)^N \tag{160}$$

μ	P_N	$P_{S,left}$	$P_{S,right}$	P_D
0	0.97	0.016	0.016	9.9e-05
50	0.189	–	0.248	0.316
100	0.036	–	0.155	0.655
300	0.	–	0.007	0.986

Figure 70: No tag, single tag on the left or right side (same by definition) and double tagged probablity.

The hit probabilities can then be calculated for various pile up values (see Fig. 70). For a pile up μ =50 (100) for instance, the probability of no tag is 19% (3.6%). Let us note that this simplified approach does not work at very high pile up (300 for instance) since we neglected the cases when two or more protons from pile up events can hit one side of the detector at the same time. In order to illustrate this, the percentage of events corresponding to 0, 1, 2, 3... protons on one side for μ =50, 100 and 300 is given in Fig. 71. This leads to larger inefficiencies that can be taken account in a more refined approach or by a full pile up simulation, which was performed for the $\gamma\gamma\gamma\gamma$ quartic anomalous coupling study. The detector needed to detect intact protons has a coverage of about 2 cm×2 cm and is located 15σ from the beam. The inefficiency of such a detector assuming 20×8 pixels is given in Fig. 72. The numbers displayed in the table correspond to the probability of getting one proton or more in a given pixel for μ =100 or a 20×8 pixellised detector. The upper limit on the inefficiencies if the order of 8% for the pixels closest to the bins, but is found negligible for pixels further away which measure higher mass diffractive objects. For comparison, the inefficiences for μ =50 is about half, and vertical bar detectors lead to larger inefficiencies between 10 and 20% on a large part of the detector (a 7 bar detector with 2 mm width for the first bar and 3.25 mm for other bars, leads to inefficiences

betweem 8% and 19% for the first 6 bars). It is also worth mentioning that this study only includes physics backgrounds and not beam-induced backgrounds which are not in the simulation. Recent results from TOTEM show that the beam-induced backgrounds have the tendency to be high and located in the pixels closest to the beam [45], and this is why a full pixelised detector is preferable to bars.

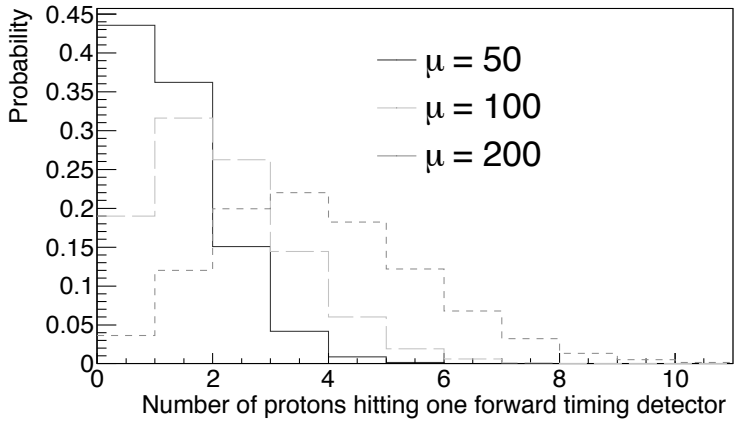

Figure 71: Probability of getting 0, 1, 2, 3... intact protons on one side of the detector for 3 different values of μ.

Inefficiencies - 20x8 pixel design - μ = 100										
Row/Column	1	2	3	4	5	6	7	8	9	10
8	0.	0.	0.	0.	0.	0.	0.	0.	0.	0.
7	0.	0.	0.	0.	0.	0.	0.	0.	0.	0.
6	0.038	0.002	0.	0.	0.	0.	0.	0.	0.	0.
5	0.067	0.077	0.051	0.006	0.001	0.001	0.001	0.001	0.001	0.
4	0.001	0.001	0.015	0.049	0.042	0.024	0.012	0.006	0.004	0.003
3	0.	0.	0.	0.001	0.007	0.019	0.022	0.018	0.013	0.008
2	0.	0.	0.	0.	0.	0.002	0.006	0.010	0.012	0.011
1	0.	0.	0.	0.	0.	0.	0.001	0.003	0.005	0.007
Row/Column	11	12	13	14	15	16	17	18	19	20
8	0.	0.	0.	0.	0.	0.	0.	0.	0.	0.
7	0.	0.	0.	0.	0.	0.	0.	0.	0.	0.
6	0.	0.	0.	0.	0.	0.	0.	0.	0.	0.
5	0.001	0.001	0.001	0.001	0.001	0.	0.	0.	0.	0.
4	0.002	0.002	0.001	0.001	0.001	0.001	0.001	0.001	0.001	0.
3	0.006	0.004	0.003	0.003	0.002	0.002	0.001	0.001	0.001	0.
2	0.010	0.008	0.006	0.004	0.004	0.003	0.003	0.002	0.002	0.
1	0.008	0.008	0.007	0.006	0.005	0.004	0.004	0.003	0.003	0.

Figure 72: Probability of more than 1 proton to fall in a given pixel of the timing detector.

7 The SAMPIC chip

7.1 Introduction: Timing measurements in particle physics and in medical imaging

In order to measure rare events at the LHC, the luminosity (or in other words the number of interactions per second) has to be as large as possible. In order to achieve this goal, the number of interactions per bunch crossing can be very large, up to 40-70 during the LHC running of 2015-2017 as an example. Timing measurements are crucial at the LHC in order to determine if the intact protons originate from the main hard interaction or from secondary ones (pile up). Measuring the proton time-of-flight with a typical precision of 10 ps allows constraining the protons to originate from the

main interaction point of the event (hard interaction) with a precision of about 2.1 mm. For a pile up of 40 (which means about 40 interactions occuring in the same bunch crossing at the LHC), such a precision on time-of-flight measurements leads to a reduction in background of a factor of about 40 [44].

Timing measurements have also many applications in drone technology and in medical imaging as an example. The "holy grail" of medical imaging would be a PET detector with a 10 ps timing precision. With such an apparatus, image reconstruction is no longer necessary (the analysis can be performed online) since many fake coincidences can be suppressed, only attenuation corrections are needed, and real time image formation can be performed.

In order to achieve a 10 ps precision, many steps are needed going from the detector to the electronics and the readout software. In this article, we will concentrate on the achievement concerning the picosecond timing electronics that is currently being done in IRFU/SEDI Saclay and in LAL-Orsay [46, 47].

7.2 SAMPIC: SAMpler for PICosecond time pick-off

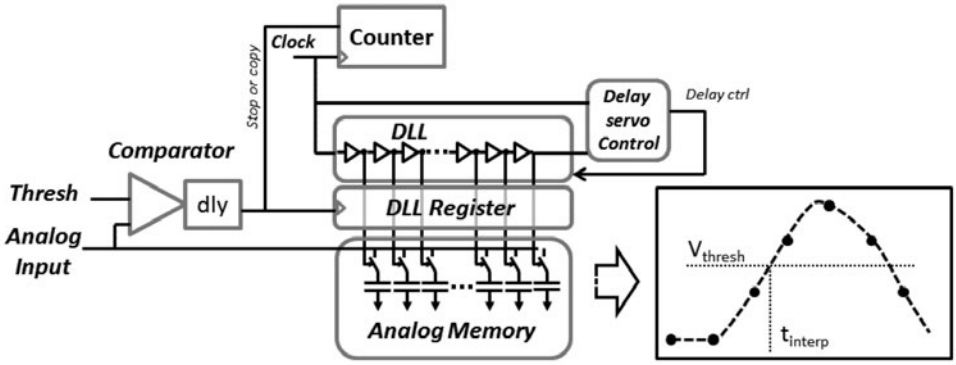

Figure 73: Scheme of the SAMPIC chip.

Figure 74: Picture of the SAMPIC chip and its acquisition board.

Before SAMPIC, the most performant Time to Digit Converters (TDCs) used digital counters and Delay Line Loops (DLLs). The timing resolution is limited by the DLL step and with most

advanced Application Specific Integrated Circuit (ASICs), one gets a resolution of about 20 ps (new developments at CERN target 5 ps). The inconvenient is that a TDC needs a digital input signal: the analog input signal has to be transformed into a digital one with a discriminator which means that the timing resolution will be given by the quadratic sum of the discriminator and the TDC timing resolutions, thus leading to worse timing resolutions.

A new approach had to be developed using the principle of a wafeform based TDC. The idea is to acquire the full waveform shape of a detector signal in an ASIC dedicated to picosecond timing measurements. The input signal range has to be between 0.1 and 1. V with a fast rising time up to 1.ns in order to get the best possible performance of SAMPIC. The present version of the chip holds 16 channels (50 Ω terminated) with independent dead time. The possible trigger modes are either self triggered or triggered externally. Each channel includes an analog memory (64 cells) and recording is triggered by a discriminator. A Gray counter associated to DLLs allows assigning a time to the different samples and an ADC provides the conversion into a digital signal.

Three timing measurements with different precision are performed in SAMPIC. The time stamp Gray counter has a 6 ns step (it samples the reference clock), the DLL 150 ps (it defines a region of interest) and the waveform shape a few ps RMS after interpolation between the acquired points (they are acquired on a 64 step analog memory).

As we already mentioned, SAMPIC acquires the full waveform shape of a detector signal. The discriminator is used only for triggering, not for timing, and thus there is no jitter originating from the discriminator. All the information concerning the signal is kept in SAMPIC, and it is possible to use offline signal processing algorithms in order to improve the timing resolution. It can also be used to obtain other signal characteristics such as the deposited charge. In the present version, SAMPIC suffers an important dead time per channel due to the ADC conversion of about 1 μs. It will be reduced by about one order a magnitude in the next version of SAMPIC, using in particular the so called "ping-pong" method and analog buffering. Two SAMPIC chips can be hosted in a mezzanine board developed in LAL, Orsay, leading to a 32-channel system. The input into SAMPIC is sent via MCX connectors. SAMPIC can be read out using an USB-Ethernet-Optic fiber readout is also provided. A 5 V voltage power supply is the only element needed to run the mezzanine board and the readout software runs on Windows or Linux. A scheme of SAMPIC is given in Fig. 74 and a picture of SAMPIC together with its acquisition board in Fig. 72.

SAMPIC is quite cheap (about 10 Euros per channel) with respect to a few 1000s Euros for previous technology, which means that it can be used in large scale detectors such as PET for medical applications.

As a reference, a table giving the parameters of the SAMPIC chip is given in Fig. 75.

7.3 SAMPIC performance

Electronics tests

In this section, we describe the SAMPIC performance obtained from pure electronics tests. The maximum signal size is about 1.V, and after corrections, the average noise is quite low, of about 1 mV RMS (the noisiest cells being 1.5 mV RMS), which means a dynamic 10 bits RMS.

The SAMPIC cross talk was measured by sending a signal of 800 mV with a 300 ps rise time on one channel and reading out the neighbouring channels. The cross talk was found to be less than 1%. The quality of sampling was tested using a sinus wave signal, and the signal was perfectly reproduced without corrections at a sampling frequency of 10 Gigasamples per second. The sampling speed in SAMPIC is possible between 3 and 8.2 Gigasamples per second on 16 channels (up to 10 Gigasamples per second for 8 channels).

The timing resolution was studied by using two different channels of SAMPIC. The same signal was sent on both channels, one being delayed compared to the other one using a delay box or longer cables. The pulse had an amplitude of about 1.2 V, and we used the 6.4 Gigasamples per second

		Unit
Technology	AMS CMOS 0.18µm	
Number of channels	16	
Power consumption	180 (1.8V supply)	mW
Discriminator noise	2	mV rms
SCA depth	64	Cells
Sampling Speed	<3-8.4 (10.2 for 8 channels only)	GSPS
Bandwidth	1.6	GHz
Range (Unipolar)	1	V
ADC resolution	8 to 11 (trade-off time/resolution)	bit
SCA noise	<1.3	mV rms
Dynamic range	9.6	Bit rms
Conversion time	0.2-1.6 (8bit-11bit)	µs
Readout time (can be probably be /2)	25 + 6.2/sample	ns
Time precision before correction	15	ps rms
Time precision after timing INL correction	< 5	ps rms

Figure 75: Parameters of the SAMPIC chip.

configuration. The RMS of the time difference between the two signals as a function of delay is given in Fig. 76 using two different offline algorithms to reconstruct the time difference (CDF as constant fraction discriminator and CC as cross correlation using a linear or a spline interpolation between the different points measured by SAMPIC). The time resolution is quite flat as a function of the delay between the two signals and is about 5 ps, leading to a time resolution per channel of about 4 ps.

A similar study of the timing resolution versus the signal amplitude is shown in Fig. 77. The signal has to be above 450 mV in order to obtain the best timing resolution possible of about 4 ps.

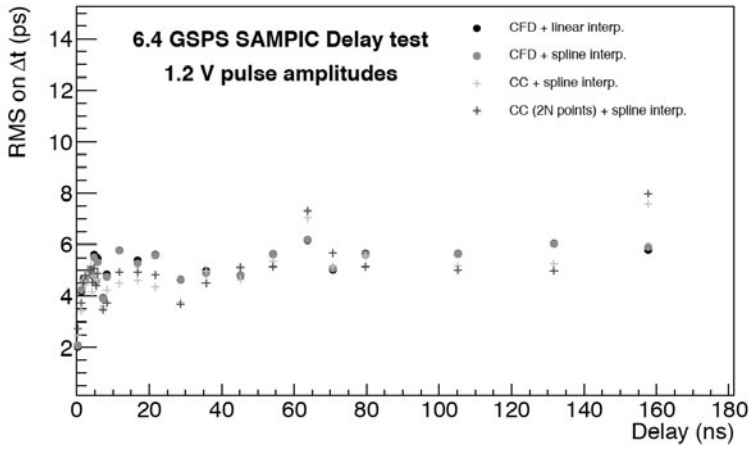

Figure 76: RMS on the time difference between two signals, one being delayed with respect to the other using two offline algorithms (Constant Fraction Discriminator (CFD) and cross correlation (CC)) using a linear or a spline interpolation.

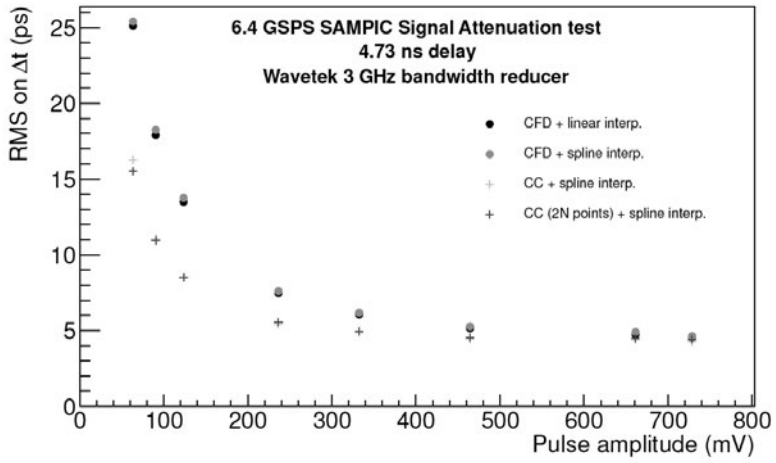

Figure 77: RMS on the time difference between two signals as a function of the signal amplitude using two offline algorithms (Constant Fraction Discriminator (CFD) and cross correlation (CC)) using a linear or a spline interpolation.

Timing resolution using detectors

The second series of tests was performed by plugging SAMPIC into a real detector. We used a laser signal splitted in two, and going through two fast Si detectors [11]. The time difference between the two channels was measured using SAMPIC. The result is shown in Fig. 78 using the offline cross correlation algorithm. The time resolution is about 30 ps. It is of course dominated by the fast Si detectors, the resolution of SAMPIC being of the order of 4 ps. Additional studies are being performed in beam tests using diamond detectors leading to a time resolution of 80 to 90 ps [48].

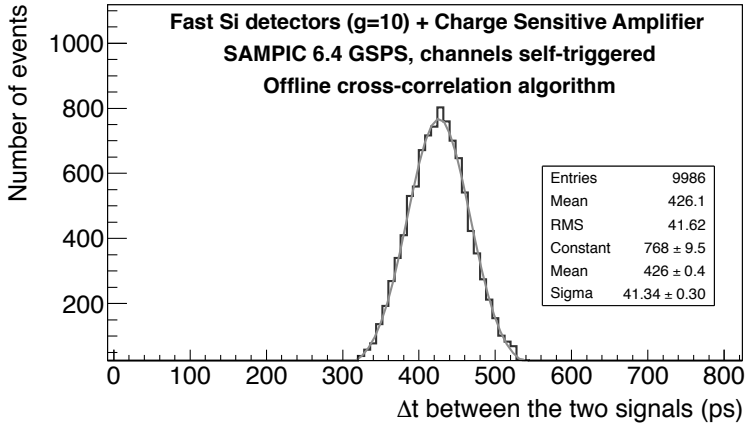

Figure 78: Time difference between two SAMPIC channels reading out Si detectors, a laser signal splitted in two going through the two Si detectors.

7.4 Conclusion

A self triggered timing chip demonstrator has been designed and characterised with 1.6 GHz bandwidth, up to 10 Gigasamples per second, low noise and of the order of 4 ps timing resolution. The chip is now ready and can be used for tests. Tests already started within the AFP, CT-PPS and CMS/TOTEM projects using quartz, diamond and Si detectors. Work is still going on in order to improve the chip concerning the DAQ system optimisation (firmware and software) and the improve-

ment of the dead time using the "ping-pong" method. SAMPIC can now be used in many applications for tests in addition to particle physics for instance in medical imaging, drones, in detectors including many channels due to the low cost per channel.

8 Conclusion

In these lectures, we described some topics related to diffraction at the LHC going from soft diffraction to hard inclusive, exclusive diffraction and to photon-exchange processes. We finished by describing the experimental setup that is being built by the CMS, TOTEM and ATLAS collaborations.

Acknowledgments

The write up of these lectures was based on many publications and proceedings with my collaborators and I would like to thank D. Breton, V. de Caqueray, N. Cartiglia, E. Chapon, E. Delagnes, S. Fichet, G. von Gersdorff, H. Grabas, Y. Hatta, O. Kepka, J. Maalmi, C. Marquet, N. Minafra, R. Peschanski, M. Saimpert, L. Schoeffel, G. Soyez, R. Staszewski, M. Trzebinski, D. Werder...

References

1. J. C. Collins, Phys. Rev. D **57**, 3051 (1998) [Erratum: Phys. Rev. D **61**, 019902 (2000)] [hep-ph/9709499 [hep-ph]].
2. A. Aktas *et al.* [H1 Collaboration], Eur. Phys. J. C **48**, 715 (2006) [hep-ex/0606004 [hep-ex]].
3. A. Aktas *et al.* [H1 Collaboration], Eur. Phys. J. C **48**, 749 (2006) [hep-ex/0606003 [hep-ex]].
4. C. Adloff *et al.* [H1 Collaboration], Z. Phys. C **76**, 613 (1997) [hep-ex/9708016 [hep-ex]].
5. C. Royon, L. Schoeffel, S. Sapeta, R. B. Peschanski and E. Sauvan, Nucl. Phys. B **781**, 1 (2007) [hep-ph/0609291 [hep-ph]]; C. Royon, L. Schoeffel, R. B. Peschanski and E. Sauvan, Nucl. Phys. B **746**, 15 (2006) [hep-ph/0602228 [hep-ph]].
6. G. Altarelli and G. Parisi, Nucl. Phys. B **126**, 298 (1977); V. N. Gribov and L. N. Lipatov, Sov. J. Nucl. Phys. **15**, 438 (1972) [Yad. Fiz. **15**, 781 (1972)]; V. N. Gribov and L. N. Lipatov, Sov. J. Nucl. Phys. **15**, 675 (1972) [Yad. Fiz. **15**, 1218 (1972)]; Y. L. Dokshitzer, Sov. Phys. JETP **46**, 641 (1977) [Zh. Eksp. Teor. Fiz. **73**, 1216 (1977)].
7. *Report from the LHC Forward Physics Working Group*, edited by N. Cartiglia and C. Royon (2015).
8. http://hep.fi.infn.it/LHCf [LHCf Collaboration].
9. http://lhcb.web.cern.ch/lhcb/Physics-Results/LHCb-Physics-Results [LHCb Collaboration].
10. https://twiki.cern.ch/twiki/bin/view/ALICEpublic /ALICEPublicResults [ALICE Collaboration].
11. C. Royon and N. Cartiglia, Int. J. Mod. Phys. A **29**, 1446017 (2014); N. Cartiglia, in Proceedings of the workshop on timing detectors, Clermont-Ferrand (2014).
12. ATLAS Collaboration, report CERN-LHCC-2011-012; TOTEM Collaboration, report CERN-LHCC-2014-020; CMS and TOTEM Collaborations, report CERN-LHCC-2014-021.
13. T. Martin, in CERN yellow report on LHC Forward Physics, to be published.
14. C. Royon, these proceedings.
15. R. Aaij *et al.* [LHCb Collaboration], J. Phys. G **41**(11), 115002 (2014) [arXiv:1407.5973 [hep-ex]].
16. https://twiki.cern.ch/twiki/bin/view/LHCb/PrelimExclDiMu [LHCb Collaboration].
17. V. A. Khoze, A. D. Martin and M. G. Ryskin, Eur. Phys. J. C **23**, 311 (2002) [hep-ph/0111078 [hep-ph]].
18. U. Maor, these proceedings.

19. http://totem-experiment.web.cern.ch/totem-experiment [TOTEM Collaboration]; http://atlas.cern [ATLAS Collaboration].
20. S. Fichet, G. von Gersdorff, O. Kepka, B. Lenzi, C. Royon and M. Saimpert, Phys. Rev. D **89**, 114004 (2014) [arXiv:1312.5153 [hep-ph]]; S. Fichet, G. von Gersdorff, B. Lenzi, C. Royon and M. Saimpert, JHEP **1502**, 165 (2015) [arXiv:1411.6629 [hep-ph]].
21. E. Chapon, C. Royon and O. Kepka, Phys. Rev. D **81**, 074003 (2010) [arXiv:0912.5161 [hep-ph]]; O. Kepka and C. Royon, Phys. Rev. D **78**, 073005 (2008) [arXiv:0808.0322 [hep-ph]].
22. D. d'Enterria and G. G. da Silveira, Phys. Rev. Lett. **111**, 080405 (2013) [Erratum: Phys. Rev. Lett. **116**(12), 129901 (2016)][arXiv:1305.7142 [hep-ph]]; H. Sun, Eur. Phys. J. C **74**(8), 2977 (2014) [arXiv:1406.3897 [hep-ph]].
23. M. Boonekamp, A. Dechambre, V. Juranek, O. Kepka, M. Rangel, C. Royon and R. Staszewski, arXiv:1102.2531 [hep-ph]; M. Boonekamp, V. Juranek, O. Kepka and C. Royon, in "*Proceedings of the workshop: HERA and the LHC workshop series on the implications of HERA for LHC physics,*" arXiv:0903.3861 [hep-ph].
24. E. Chapon, C. Royon and O. Kepka, Phys. Rev. D **81**, 074003 (2010) [arXiv:0912.5161 [hep-ph]]; J. de Favereau de Jeneret *et al.*, arXiv:0908.2020 [hep-ph].
25. O. Kepka and C. Royon, Phys. Rev. D **78**, 073005 (2008) [arXiv:0808.0322 [hep-ph]].
26. G. Belanger and F. Boudjema, Phys. Lett. B **288**, 201 (1992).
27. G. Abbiendi *et al.* [OPAL Collaboration], Phys. Rev. D **70**, 032005 (2004) [hep-ex/0402021 [hep-ex]].
28. S. Chatrchyan *et al.* [CMS Collaboration], JHEP **1307**, 116 (2013) [arXiv:1305.5596 [hep-ex]]; V. M. Abazov *et al.* [D0 Collaboration], Phys. Rev. D **88**, 012005 (2013) [arXiv:1305.1258 [hep-ex]].
29. ATLAS Collaboration, report CERN-LHCC-2011-012; M. G. Albrow [CMS and TOTEM Collaborations], PoS DIS **2015** (2015) 064.
30. S. Fichet and G. von Gersdorff, JHEP **1403**, 102 (2014) [arXiv:1311.6815 [hep-ph]]; R. S. Gupta, Phys. Rev. D **85**, 014006 (2012) [arXiv:1111.3354 [hep-ph]].
31. L. Randall and R. Sundrum, Phys. Rev. Lett. **83**, 3370 (1999) [hep-ph/9905221 [hep-ph]].
32. ATL-PHYS-PUB-2013-009, ATLAS Collaboration; G. Aad *et al.* [ATLAS Collaboration], JINST **3**, S08003 (2008).
33. J. Monk and A. Pilkington, Comput. Phys. Commun. **175**, 232 (2006) [hep-ph/0502077 [hep-ph]]; V. A. Khoze, A. D. Martin and M. G. Ryskin, Eur. Phys. J. C **55**, 363 (2008) [arXiv:0802.0177 [hep-ph]].
34. G. Corcella, I. G. Knowles, G. Marchesini, S. Moretti, K. Odagiri, P. Richardson, M. H. Seymour and B. R. Webber, hep-ph/0210213 [hep-ph].
35. T. Sjostrand, S. Mrenna and P. Z. Skands, Comput. Phys. Commun. **178**, 852 (2008) [arXiv:0710.3820 [hep-ph]].
36. A. Aspect, P. Grangier and G. Roger, Phys. Rev. Lett. **49**, 91 (1982); A. Aspect, J. Dalibard and G. Roger, Phys. Rev. Lett. **49**, 1804 (1982).
37. K. Piotrzkowski, U. Schneekloth, in Proc. of the ZEUS Collaboration meeting, DESY, Hamburg (1994).
38. ATLAS IBL Collaboration, report CERN-LHCC-2010-013 [ATLAS-TDR-019 5/09/2010].
39. H. C. Kästli, Nucl. Instrum. Meth. A **731**, 88 (2013).
40. CMS Collaboration, report CERN-LHCC-2012-016; CMS Collaboration, report CMS-TDR-11.
41. A. Brandt, in Microchannel Plate PMT Lifetime and Performance, DIRC2011: Workshop on Fast Cerenkov detectors, Giessen (2011).
42. CMS Collaboration, report CERN-LHCC-2012-015; CMS Collaboration, report CMS-TDR-010.
43. G. Chiodini, in Proceedings of the workshop on timing detectors, Clermont-Ferrand (2014).
44. C. Royon, M. Saimpert, O. Kepka, R. Žlebčík, Acta Phys. Polon. B, Proceedings supplement, **7**(4), 735 (2014).

45. M. Beretti, talk given at *LHC Working Group on Forward Physics and Diffraction*, Trento (2014).
46. E. Delagnes, H. Grabas, D. Breton, J. Maalmi, P. Rusquart, Acta Phys. Polon. B, Proceedings supplement, **7**(4), 685 (2014).
47. D. Breton, E. Delagnes, J. Maalmi, P. Rusquart, Acta Phys. Polon. B, Proceedings supplement, **7**(4), 685 (2014).
48. Beam tests performed at CERN/DESY [TOTEM Collaboration], private communication.